# Selection and Characterisation of the Target Fault for Fluid-Induced Activation and Earthquake Rupture Experiments

Peter Achtziger-Zupančič [1,2,*], Alberto Ceccato [3], Alba Simona Zappone [3], Giacomo Pozzi [4], Alexis Shakas [3], Florian Amann [1,2], Whitney Maria Behr [3], Daniel Escallon Botero [3], Domenico Giardini [3], Marian Hertrich [3], Mohammadreza Jalali [2*], Xiaodong Ma [5], Men-Andrin Meier [3], Julian Osten [2], Stefan Wiemer [3], and Massimo Cocco [4]

[1]Fraunhofer Research Institution for Energy Infrastructures and Geothermal Systems IEG, Aachen, Germany
[2]Department of Engineering Geology and Hydrogeology, RWTH Aachen University, Germany
[3]Department of Earth Sciences, ETH Zurich, Switzerland
[4]Istituto Nazionale di Geofisica e Vulcanologia, Italy
[5]School of Earth and Space Sciences, University of Science and Technology of China, Hefei, China
[*]Corresponding authors (peter.achtziger-zupancic@ieg.fraunhofer.de, jalali@lih.rwth-aachen.de)

**Abstract.** Performing stimulation experiments at approximately 1 km depth in the Bedretto Underground Laboratory for Geosciences and Geoenergies necessitates identifying and characterizing the target fault zone for on-fault monitoring of induced fault-slip and seismicity, a current challenge in understanding seismogenic processes. We discuss the multidisciplinary approach for selecting the target fault zone for the experiments planned within the Fault Activation and Earthquake Ruptures

5 (FEAR) project, aiming to induce fault-slip and seismicity up to a magnitude 1.0 earthquake while enhancing monitoring and control of fluid-injection experiments.

Structural geological mapping, remote sensing, exploration drilling and borehole logging, ground-penetration radar, and laboratory investigations were employed to identify and characterize the target fault — a ductile-brittle shear zone several meters wide with intensely fractured volume persisting over 10 m. Its orientation in the in-situ stress field favors reactivation in

10 normal to strike-slip regimes. Laboratory tests showed slight velocity strengthening of the fault gouge. The fault's architecture, typical for crystalline environments, poses challenges for fluid flow, necessitating detailed hydraulic and stress characterization before each of the FEAR experiments. This multidisciplinary approach was crucial for managing rock volume heterogeneity and understand implications for the dense monitoring network. Successfully identifying the fault sets the stage for seismic activation experiments commencing in spring 2024.

## 1 Introduction

Earthquakes are a natural hazard affecting millions of people every year over the globe. Earthquakes are caused by complex physical and chemical processes that are not yet well understood because they involve very different spatial and temporal scales ranging from $\mu$m to $km$ and seconds to years. Our current understanding is limited by collecting high-quality multidisciplinary data near the causative faults. Indeed, most of the earthquakes nucleate at a depth of several kilometers. The waves propagating

20 from the source are scattered and attenuated during their travel to the Earth's surface, thus losing parts of the information on the rupture process. Scientists face the challenge of extracting information about the causative physical mechanisms from far-field data, with limited resolution and large uncertainties of the fault zone processes. Thus, despite advances in scientific research, many fundamental aspects of the earthquake process are still poorly understood. How earthquakes initiate and nucleate, which signals can be used as precursors of seismic events, how far a rupture propagates, when and why co-seismic rupture stops

25 propagating: they are still unresolved questions. As a result, earthquake prediction is still extremely difficult and hazard assessment is limited, particularly at close distances from the causative fault. This lack of knowledge also reduces the ability to control earthquakes related to anthropogenic underground activities, such as mining, injection of waste fluids, and stimulation of reservoirs for enhanced geothermal systems.

Laboratory experiments aimed at reproducing conditions at crustal depths on rock samples also provide observational data on

30 dynamic ruptures, fault rheology and frictional properties. Notably, this approach is limited by the size of the samples, which is often a few centimeters only, and by the applied stress and strain conditions.

Deep boreholes intersecting fault zones have been used for many decades to collect near-fault data and study the mechanisms that nucleate or trigger earthquakes, determine rupture propagation, and control the scaling of source parameters with magnitude and depth. A few projects with high scientific impact for this research (non-conclusive list) are, e.g. the German

35 Continental Deep Drilling Programme (known as Kontinentales Tiefbohrprogramm der Bundesrepublik Deutschland or KTB; Shapiro et al., 2006), the San Andreas Fault Observatory at Depth (SAFOD) in California (Zoback et al., 2011), the Taiwan Chelungpu-fault Drilling Project (TCDP; Ma et al., 2006), the Deep Fault Drilling Project (DFDP-1) in the Alpine Fault, New Zealand (Sutherland et al., 2012), the Geophysical borehole Observatory at the North Anatolian Fault (GONAF) in Turkey (Kiliç et al., 2020), and the Integrated Ocean Drilling Program (IODP) in the Nankai subduction zone of south-western Japan

40 (Tobin et al., 2022). Without diminishing the important discoveries made, these experiments were restricted to collecting direct observations from a small portion of the respective fault zone and the analysis of drill cores.

Another approach to observing earthquake nucleation directly, is to conduct experiments in underground laboratories (URL) at a scale approaching that of natural seismic events. For many decades, research dealing with the safety of radioactive waste storage and the sealing integrity of the host rock has addressed fault slip and seismicity, both natural and induced, to understand

45 reduced containment capability by increased permeability in the host rock formations. Many fault stimulation experiments have been carried out in URL hosted by low permeable sedimentary and low-porosity basement rocks. The Rustrel Low Noise Underground Laboratory (LSBB URL) in SE of France offers the possibility to access a 500 m long strike-slip to normal fault, cutting through grainstone carbonate layers at c.a. 280 m depth (Guglielmi et al., 2015a; Jeanne et al., 2012). The Tournemire

Underground Laboratory, also in France, located at 250m depth, allows the access to a strike slip fault in shales (Guglielmi
50 et al., 2015b). The Mont Terri Underground Laboratory hosted in shales at a depth of approximately 300 m, in NW Switzerland
consists of various galleries and boreholes, some of which intersect a few meters thick thrust fault (Guglielmi et al., 2015b).
All these fault reactivation experiments have been conducted as fault stimulations by water injection while monitoring their
slip and eventual associated microseismic events (Guglielmi et al., 2015a, 2017, 2020; Kakurina et al., 2019).

More recently, the growing interest in deep geothermal energy, as an alternative carbon-free energy source, has sparked re-
55 search on seismicity induced by fluid injections that are required to create an underground heat exchanger. The Underground
Laboratories that are of interest in this case are located in rocks representative of a crystalline bedrock, e.g. in plutonic or meta-
morphic formations. Research activities in accessible underground rock labs in these rocks are either in abandoned laboratories
for deep geological repository of nuclear waste, such as Whiteshell URL (Canada; e.g., Ophori et al., 1995) or Mizunami URL
(Japan; e.g., Sakuma et al., 1998), or are currently performed only at few hundred meters depth such as Äspö (Sweden at 500
60 m depth; e.g., Kickmaier and McKinley, 1997), Onkalo (Finland at 450 m depth; e.g., Siren, 2017), KURT (South Korea at
200 m depth; e.g., Kim et al., 2017), Bukov (Czech Republic at 550 m depth; e.g., Bukovská et al., 2019) or Grimsel Test
Site (Switzerland; e.g., Vomvoris et al., 2004). The latter is located at 450 metres depth in the Aar Massif, one of the External
Crystalline Massifs that represents the basement of the Alps (Schneeberger et al., 2019). The Grimsel orthogneiss hosts ductile
shear zones reactivated in the brittle field up to very recent times (Kralik et al., 1992). Since 2016 a rock volume of approx.
65 20X20X20 $m^3$ has been the target for a range of hydraulic shearing and fracturing tests, performed in injection boreholes
intersecting the shear zones (Amann et al., 2018; Jalali et al., 2018; Dutler et al., 2019, 2021; Gischig et al., 2019; Krietsch
et al., 2020a, b; Villiger et al., 2020, 2021).

All the examples above offer direct access to faults at a depth in the range of a few hundred meters, a depth that is at least one
order of magnitude too small for representing seismogenic depths. Underground laboratories situated at depths of the order
70 of kilometers are quite rare and hard to access. Deep mines offer the opportunity to compare in-situ stress variations and in-
duced seismicity. Many large mines operate extensive seismic monitoring systems as a safety measure for the mine operation.
For example, the JAGUARS (Japanese-German Acoustic Emission Research in South Africa) project continuously monitors
microseismic activity at 3.5km depth in the Mponeng gold mine, South Africa (Kwiatek et al., 2011). Data from these moni-
toring systems provide relevant information on the key features of earthquake sources. Monitoring systems can remain active
75 even when mining activities are stopped, making abandoned or partially abandoned deep mines potential deep laboratories.
The Sanford Underground Research Facility in South Dakota, located at the former site of the Homestake Gold Mine, is an
example of a very deep (up to 1490 m) underground facility (Lesko, 2015). Hydraulic fracturing and shearing experiments,
including strain monitoring have been carried out at a depth of 1500 m in a phyllitic series in recent years (Guglielmi et al.,
2021).
80 In this panorama of experimental approaches (in boreholes, underground labs, deep mines) aiming to make observations as
close to the earthquake source as possible, the Bedretto Underground Laboratory for Geosciences and Geoenergies (BULGG)
in the Swiss Alps offers an ideal experimental environment that the "Fault Activation and Earthquake Rupture" project (FEAR)
is ready to capitalize on. The BULGG is located in the central section of a 5211 m long tunnel and provides easy access to

a large volume of crystalline faulted rocks at a depth of 1000-1500m (Fig. 1) (Ma et al., 2022). The FEAR project aims to

85 reactivate, in a controlled way, a natural fault occurring at relevant depth, and observe the nucleation of a Magnitude 1 event with the most updated, complete and sophisticated instruments on the fault and surrounding rock volume. The FEAR project is described in detail in (Meier, 2024) and here we briefly summarize the aspects relevant to fault zone selection. FEAR aims to (i) perform controlled 50-100 m scale fault stimulation experiments in the basement rock at over 1000m depth, (ii) pre-condition the stress distribution on the fault to perform real-time tests of different physical sources and forecasting hypotheses, (iii) de-

90 ploy data-driven approaches and real-time modelling to conduct structured prospective forecasting experiments, (iv) integrate and validate results from deep-underground experiments, experimental rock-deformation laboratories, numerical simulations and dynamic rupture modeling, and observations from natural earthquakes. For the experiment a new dedicated tunnel will be excavated, parallel to the target fault for 125 m, at a distance of approx. 50 m (Fig. 2). The tunnel is intended to provide close-range, extensive instrumentation to monitor the experiments. FEAR, carried out by ETH Zurich, INGV Rome, and

95 RWTH Aachen University, is a pproject funded by the European Commission through a European Research Council (ERC) Synergy grant. The ERC Synergy framework enables bringing together the key complementary expertise and experiences for in-situ, lab and modelling experiments in Europe and to integrate them into a coherent research program. FEAR aims at integrating fault mechanics, seismology and numerical modeling across scales, from laboratory to deep underground experiments to natural earthquakes (Meier, 2024). The objectives of FEAR require to target a fault with specific characteristics, such as

100 favourable geometrical orientation within the local stress field, continuity of the fault for hundreds of meters, limited water inflows to the tunnel (dripping), homogeneity and isotropy of the host rock volume, indication of past seismogenic activity. The overarching goal of FEAR is to stimulate by fluid injections, an extremely well-identified and characterized fault zone and to monitor slip episodes, strain perturbation and localization, stress changes, seismicity and pressure evolution in the target volume at significant seismogenic depths (Meier, 2024). The entire FEAR experimental design depends on the identification

105 and characterization of the target fault zone and its complexity.

The goal of this paper is to present and discuss the multidisciplinary approach adopted to identify the target fault zone for the FEAR experiments. We first summarize the available information on the site selected for the underground research facility, i.e., the Bedretto tunnel. Then we present a list of constraints and criteria, resulting from the experimental requirements that we applied to the selection of the target fault zone. Consequently, we describe the data and parameters we analyzed in the site in-

110 vestigation program. We present the novel collection of observations and their interpretation used to constrain the architecture, geometry and other key properties of the selected fault zone.

## 2 Site description

### 2.1 The Bedretto Tunnel and the Bedretto Underground Laboratory for Geoenergies and Georesources

The Bedretto tunnel is located near the Gotthard Pass in the Swiss Central Alps. The Bedretto tunnel is oriented N43°W, and

115 it connects the Furka Base Tunnel on the Matterhorn Gotthard Railway line with the Bedretto Valley (Fig. 1a). A detailed description of the tunnel is available in Ma et al. (2022). The 5221 m long tunnel is entirely in crystalline rocks of the Helvetic
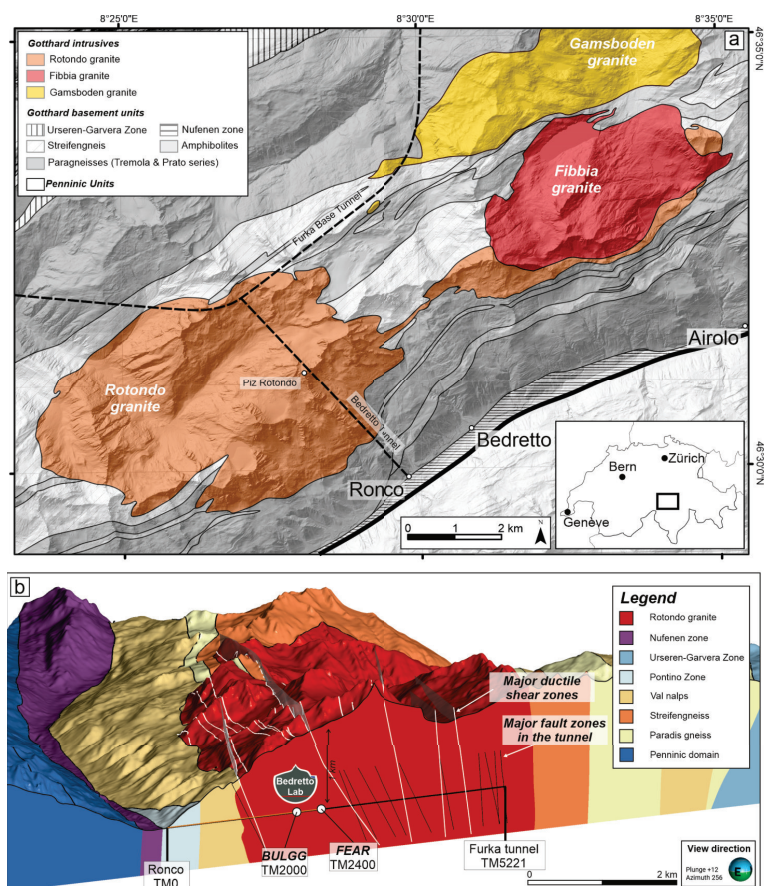
**Figure 1.** (a) Schematic geological map showing the location of the Bedretto Tunnel in the Rotondo granite. (b) 3D Geologic cross section along the Bedretto Tunnel highlighting the main geological features of the Rotondo granite.

domain and generally unsupported, allowing continuous and direct access to the rock walls. For about 4 km it crosscuts the almost undeformed Rotondo granite (Fig.1, (Hafner et al., 1975; Rast et al., 2022). Since its construction between 1971 and 1982, the tunnel was surveyed for geotechnical relevant structures by Hafner et al. (1975); Schneider (1985); Lützenkirchen and Loew (2011).

120

## 2.2   Geology

The Rotondo granite is one of the major Post-Variscan granite intrusions characterizing the Gotthard massif (Berger et al., 2017). The host rock consists of polymetamorphic paragneisses, migmatites, and amphibolites of the Tremola and Prato series (Berger et al., 2017; Rast et al., 2022). The Rotondo intrusion is mainly composed of two granitic bodies of Early Permian
125  age (295 Ma; Rast et al., 2022), the younger equigranular Rotondo granite (RG1), intruding the older porphyritic Rotondo granite (RG2). The latter RG2 is only observed in the tunnel, where it crops out between TM2805 and TM3437. After the emplacement of the Rotondo granite, the Gotthard massif underwent extensional tectonics related to the incipient opening of the Paleo-Tethys ocean in Permian-to-Jurassic times (Guillot and Ménot, 2009). During the Eocene to Miocene, the Gotthard massif was involved in the Alpine orogeny (Rast et al., 2022; Herwegh et al., 2017, 2020). During the Alpine convergence and
130  subduction, the Gotthard massif reached peak metamorphic conditions larger than 550 °C and 0.9 GPa at 20-30 Ma (Ceccato et al., 2024). The following Alpine continental collision led to fast exhumation of the Gotthard massif at 18-19 Ma (Ceccato et al., 2024). During this tectonic phase, the main set of NE-SW and ENE-WSW-trending, ductile shear zones formed in the Rotondo granite at 520 °C and 0.8 GPa. This set of ductile shear zones localized on a pre-existent set of brittle faults and shear fractures (Ceccato et al., 2024). The following ductile-to-brittle evolution of the massif during exhumation and cooling
135  was dominated by strike-slip tectonics, leading to the development of mainly dextral ductile-to-brittle shear zones and major brittle fault zones from 12 to 5 Ma (Kralik et al., 1992; Pleuger et al., 2012). These late stages of strike-slip tectonics at upper crustal conditions (T < 200 °C, depth < 7 km) led to the development of zeolite- and gouge-bearing fault zones, localizing on pre-existent ductile shear zones and shear fractures (Lützenkirchen and Loew, 2011). Tectonic structures, such as ductile shear zones and faults, especially those in the host paragneisses, have been exploited during Neogene as nucleation sites for toppling
140  zones and deep-seated gravitational slope movements (Fig. 1b; Ustaszewski et al., 2008).

## 3   The FEAR Project and the Required Fault Properties

A complex geological history such as described above results in a wide variety of ductile, ductile to brittle, and brittle discontinuities. This means a set of criteria has to be established for the identification of a suitable "target" fault zone to effectively use available resources and maximize the outcome of planned activities.

145  **The FEAR Project characteristics.** The primary objective of FEAR is to induce seismic activity (with maximum approximate magnitude $M_w = 1.0$) through hydraulic stimulation within a natural fault zone, equipped with a multidisciplinary monitoring network with unprecedented spatial resolution and proximity to the source zone. As part of the preparatory work, we are currently excavating a 125-meter-long access tunnel that runs parallel to the selected fault zone at a lateral distance of 50 meters. Through this tunnel, we will densely equip the fault zone with a remotely controlled monitoring system that operates on multi-
150  ple scales and domains, both on and off the target fault. This will allow us to monitor parameters such as fluid pressure, strain, temperature, as well as passive and active seismic signals. The goal is for fault movement to be induced in areas where the most comprehensive monitoring capabilities exist. In a series of experiments, various fluid injection and production strategies will be employed in borehole sections to (re-)activate different segments and patches of the fault zone (Fig. 2) and scrutinize

their response to fluid stimulation.

155 Therefore, the selection criteria for the fault zone took into account the following components: (1) geometry and spatial extension of the natural fault zone; (2) the logistics, installation, and cost/efficiency/density ratios of the equipment and deployment of the monitoring system, as well as the sensitivity of the monitoring equipment; (3) hydro-mechanical characteristics and (4) geological properties of the fault zone.

**(1) Geometrical and spatial requirements.** The ideal outcome of the FEAR experiments is to provoke a controlled magnitude
160 $M_w = 1.0$ seismic event. Given that seismic magnitude scales with the areal extent of the reactivated fault patch, to generate earthquakes with magnitude $M_w = 1.0$, a fault patch of roughly 1000 m$^2$ will undergo pressurization (point source with approx. 30 m radius). Nonetheless, a larger extension of the fault patches would be ideal since we aim to reactivate the same fault zone at different locations.

Therefore, (re)activating a planar single structure that is continuous over 30 to 50 meters in length would be preferable. In
165 addition, the structure should also be favorably oriented with respect to the in-situ stress field, with a high slip tendency close to the static frictional resistance of the slipping zone (i.e., the conditions for which a fault is critically stressed). Minimal variation in terms of geometry and thickness would be required to minimize the complexity of logistics, monitoring, experimental and analytical operations. Therefore, planar, continuous structures with minor variations in orientation and extent are most favorable because they are more predictable (in terms of spatial development).

170 **(2) Monitoring requirements.** A dense monitoring network of sophisticated and accurate monitoring sensors (cementable tube pore pressure sensors, fiber-optics cable for strain and temperature monitoring, stress boreholes probes, acoustic emission sensors, high frecquency accelerometers, etc.) will be deployed to provide high resolution data within a (limited) volume around the fault zone. The aforementioned extension of 30-50 m is large enough to retrieve high-resolution data, enabling in-depth examination of the source characteristics. To maximize the effectiveness/cost ratio a geometrically predictable fault zone is
175 needed, which is large enough to generate a possible $M_w = 1.0$ earthquake but laterally limited to avoid run-away events. A predictable geometry helps to design a dedicated *ad-hoc* monitoring network with specific spatial arrangement, density, and sensitivity of the equipment in advance. A fault of limited persistence and thickness is necessary to minimize the extension of the monitoring network and the necessary equipment. Because the stressing of the fault patches will be monitored and predicted in real-time, the maximal thickness of the structure that can be instrumented and reliably monitored is limited to 1-10 m.

180 **(3) Hydraulic requirements.** The hydraulic characteristics of the fault zone play a crucial role in enabling the pressurization and inducing slip during the hydraulic stimulation experiments. The primary focus for the selection is put on the hydraulic properties, such as hydraulic conductivity (or permeability), hydraulic connectivity and in-situ fluid pressure within and surrounding the fault zone. In order to increase the hydraulic response during hydraulic stimulation, the fault permeability should be high enough to ensure the pressurization of a large volume to induce seismic slip but needs to be limited to prevent rapid
185 pressure dissipation and effective pump control (injection flow rate and pressure). Resulting low in-situ fluid pressures are indicative for fault depletion and direct connection to low-pressure zones around tunnels. With this regard, well-defined no-flow boundaries (host rock) at a distance in the range of the patch size necessary for the $M_w = 1.0$ earthquake are advantageous. In conclusion, fault zones with a wet or dripping character or those displaying some minor flow to the current Bedretto Tunnel

were considered suitable, while those with no flow or highly productive structures are unsuitable.

190 **(4) Geological requirements.** Homogeneity of the host rock is fundamental to receive optimal inversions of the seismic and hydraulic signals resulting from the experiments. Anisotropic host rocks, such as metamorphic rocks and ductile shear zones characterized by pervasive planar foliations introduce a mechanical anisotropy in the system that affects the complexity of the monitoring, analytical, experimental and modelling operations. Additionally, geological characteristics of the faults suggesting past seismic activity in geological or recent times, as well as geological characteristics favouring the nucleation and propaga-

195 tion of seismic rupture during fault (re-)activation, are preferred for the fault zone. In particular, the occurrence of granular and gouge (velocity-weakening) fault rocks (e.g., Niemeijer and Spiers, 2007; Volpe et al., 2023) were considered favourable characteristics to induce seismic fault reactivation. In addition, fault intersections were also considered in the selection. Faults offset by other discontinuities have more complex fault zone geometries, altering stresses and hydraulics locally, and therefore different slip tendencies; thus fault zones offset by younger fault sets were given lower priority.
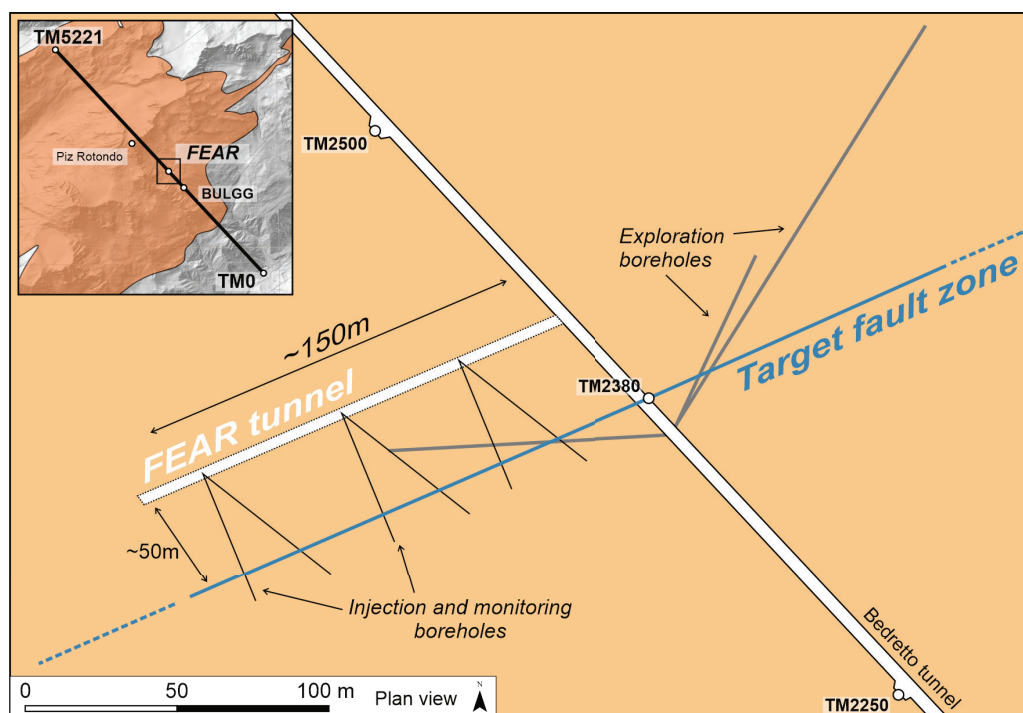
**Figure 2.** Schematic plan view on the experimental setup of the FEAR project, highlighting the Bedretto tunnel, the planned fault-parallel access tunnel (FEAR tunnel), the steeply dipping target fault zone (blue), and the planned boreholes hosting the monitoring instrumentation and the injection system.

## 4   A Multidisciplinary Approach to Fault Selection and Characterization

Following the constraints defined above, a multidisciplinary and multi-scale approach has been developed to evaluate the hundreds of faults that crop out in the Bedretto tunnel, in an effort to find the structure that best matches the criteria for the FEAR experiments. Integrated data was collected from regional to sample scale, both at the surface and in the tunnel. Methods include:

- geological characterization at the field and tunnel scale, in order to illuminate the geological characteristics of the faults in the Rotondo granite, their geometrical properties and spatial extents;

- borehole drilling, logging and core analyses;

- geophysical investigations with Ground Penetrating Radar;

- laboratory- and sample characterization;

- hydro-mechanical characterization.

The methods were applied in a three-stage process: (A) General inventory of structures in the Rotondo granite ; (B) Narrowing of the tunnel section and selection of the most suitable fault zone(s) based on the selection criteria; (C) Characterization of the fault zone(s).

**(A) Structural inventory.** The general existence of suitable structures has been analysed by remote sensing and field investigations.

- geological characterization, structural and remote sensing analysis in surface outcrops (Section 5.1, Fig. 3);

- subsurface geological and structural analyses (Section 5.2; Fig. 4);

**(B) Fault zone selection.** For finding and selecting the most suitable fault zones within the selected tunnel section a ~~selection~~ process has been applied based on:

- The tunnel sections has been constrained by general geological, logistic and operational considerations, and ongoing operations in the BULGG (Section 5.2);

- slip tendency analysis based on poles of faults (Section 5.2; Ma et al., 2022);

- GPR investigations along the tunnel wall (Section 5.2, Fig. 5).

The criteria-oriented investigations reduced the number of suitable fault zones to a few candidates.

**(C) Fault zone characterization.** The selected fault zone(s) have been characterized by an integrated analytical and methodological workflow, including:

- detailed geological and structural characterization in the tunnel (Section 5.3; Fig. 7);

- laboratory characterization of the mineralogy and microstructure of fault rocks, including experimental deformation to constrain the frictional, mechanical, and permeability properties of the fault rocks in the selected fault zone (Section 5.3; Volpe et al., 2023; Osten et al., 2024);

- drilling of exploration boreholes at an angle to the selected fault zone to constrain the actual lateral extent and continuity (Section 5.4; Fig. 6);

- logging of cores retrieved from boreholes (Section 5.4; Fig. 8);

- borehole logging adopting Acoustic and Optical Televiewer (Section 5.4; Fig. 8);

- GPR logging (Section 5.4; Fig. 9).

The final result is a preliminary geological-geometrical model of the fault zone (Section 5.5; Fig. 10), integrating all the multiscale observations resulting from multidisciplinary characterization. The proposed preliminary geometrical model is tested against synthetic GPR profiles computed with forward modelling as explained below (Section 5.6; Fig. 11). The detailed analytical techniques and methodological approaches adopted for fault zone selection and characterization are described in the following sections.

## 4.1 Remote Sensing and Geological Field Investigations in the Rotondo Granite

Large-scale remote sensing and field geological surveys were used to document the structural elements of the Rotondo massif exposed at the surface above the Bedretto Tunnel. Remote sensing analyses involved the manual interpretation of lineaments and structural features identified in multidirectional hillshade models, computed from high-resolution digital elevation models (DEM, 25 cm/pxl, SwissSURFACE3D, Swisstopo), high-resolution aerial images draped on the 3D DEM (10 cm/pxl, SwissIMAGE database, Swisstopo), and orthophotos and DEM of limited outcrops (200-400 m$^2$) obtained through local surveys with UAV-drones (0.5cm/pxl, DJI Mavic 2). The interpretation of lineaments was manually performed in ArcGIS on hillshaded DEM and aerial orthoimages. The result is a database containing the orientation (dip, strike, and dip direction) and the projected length of each element, which has been analyzed following the approach of Ceccato et al. (2022). The strike of lineaments was plotted in a moving-average rose diagram (Munro and Blenkinsop, 2012) to constrain sets with dominant orientations and the variation in relative frequencies from regional to local scale.

The field investigations focused on identifying the different deformation structures in the Rotondo granite and validating the remote sensing interpretations. The structural characterization included systematic collection of oriented and georeferenced data of planar (Dip/DipDirection) and linear (Plunge/Trend) features. The kinematics of deformation structures, the thickness of deformation zones, the mineralogy and the fabrics of relevant shear zones (mineral composition, foliations, etc.), and the cross-cutting relationship between characteristic sets of deformation structures were documented. The results of the field investigations have been compiled as a georeferenced database in Ceccato et al. (2024), with particular focus on the identification and characterization of secondary geological features, such as hydrothermal alteration of the Rotondo granite related to deformation structures, likely affecting its petrophysical/geomechanical properties.

### 4.2 Drilling, Geophysical and Core Investigations

To assess the lateral continuity, planarity, and thickness of fault zones in the tunnel a ground penetrating radar (GPR) measurement campaign has been conducted along the tunnel walls and inside the exploration boreholes BFE_A_05, _06 and _07. Both GPR systems consist of a transmitter and receiver antenna pair (developed by MALÅ - GuidelineGeo AB), which emits and records electromagnetic signals in the megahertz (MHz) range. A 160 MHz system has been used for the acquisition at the tunnel walls, and a 20 MHz and a 100 MHz system has been used in the borehole campaigns. Previous experience in BULGG demonstrated successful imaging of faults up to distances of 60 m into the rock volume caused by the strong di-electrical contrast between the intact Rotondo granite and water-bearing or gouge-filled structures (Shakas et al., 2020). Since the conditions and environment are identical to Shakas et al. (2020), we do not elaborate here on the processing steps applied to raw data and show structurally interpreted results instead.

Potential candidate fault zones have been mapped in detail by the scanline approach along the tunnel. Three sub-horizontal (approx. 10-20° downdip) exploration boreholes have been drilled to a depth of $\simeq$216 m (BFE_A_05, NE side), $\simeq$55 m (BFE_A_06, NE side), and $\simeq$101 m (BFE_A_07, SW side). The boreholes were diamond-drilled and the resulting cores were integrally documented with digital images and catalogued using a local dbase compatible with the Mobile Drilling Information System adopted by ICDP projects (Harms, 2021). Cores allowed the mapping of structural discontinuities and the identification of a small number of core facies (Fig. 8a). Five main core facies have been delineated, from F0 (intact host Rotondo granite) to F4 (altered and faulted granite).

The increasing core facies identifier, from F0 to F4, represents the increasing degree of fracturing, occurrence of open fractures or gouge-filled fractures, and the presence of hydrothermal alteration in the host granite (Fig. 8b). Increasing core facies numbering also qualitatively reflects the primary, secondary (fracture) and tertiary (dissolution) porosity and cohesion characteristics of the rock, where experience from previous boreholes show that it correlates with permeability. The facies have been correlated between the boreholes to trace the lateral continuity of structural and lithological features.

Apart from core-logging, wireline logging measurements have been conducted inside these boreholes. In addition to GPR (as described above), optical and acoustic televiewers from Advanced Logic Technology (ALT) have been deployed. The wireline-logging allowed to (a) obtain accurate measurements for the orientation of the borehole, in terms of its tilt and azimuth, along its entire depth, and (b) characterize both the orientation and type of structures that intersect the borehole. The combination of cores, televiewer imaging and borehole GPR provide a comprehensive dataset to correlate the candidate structures between the tunnel and the boreholes. In Fig. 6, the geometry of the three exploration boreholes is shown as drilled from the Bedretto tunnel.

### 4.3 Petrological, Petrophysical and Hydro-Mechanical Investigations

Lab investigations consisted of the analysis of rock mineralogy, rock fabric, frictional properties of fault gouges (cataclastic product of the high-strain fault cores), water chemistry, porosity, density, permeability and frictional properties. Physico-chemical properties of ground water (temperature, pH, and electrical conductivity) have been characterized on regularly ac-

quired samples from torrents, natural tunnel inflows, and borehole outflows (Arnet, 2022). Analyses include water composition and isotopic ratios.

295 Rock samples from field and tunnel outcrops, and from segments of borehole logs have been analyzed with thin sections and optical microscopy. Fault gouge mineralogy has been assessed using x-ray powder diffraction using a Bruker D8 Advance X-ray system provided with Lynxeye XE-T silicon-strip detector (Volpe et al., 2023). Additionally, rock deformation experiments have been conducted using the natural gouge sampled from the fault cores at TM2380 and TM2800 (Volpe et al., 2023). These experiments yielded information on the frictional properties and permeability of the sampled gouges with implications for fault

300 slip behavior during reactivation. Permeability and porosity of rocks from fault zones were measured by helium-pycnometry and water saturation methods, flow-through experiments at confined conditions, and unconfined gas permeameter measurements (Osten et al., 2024). These samples were collected at TM1590 (4 boreholes of <1m), TM2380 (4 boreholes of <1m) and TM2780 (3 boreholes of 10m). Lab investigations are briefly summarized here. The reader is referred to the published theses and referenced articles for further details.

### 4.4 Geological-Geometrical Data Integration, Geometrical Modeling and GPR-Simulations

The different datasets obtained from regional-to borehole-scale characterization of the target fault have been integrated into a 3D model to constrain the geometrical characteristics and spatial persistence of the selected target fault zone. In particular, tunnel observations, LiDAR scanning and virtual outcrop models, the distribution of fracture intensity, and core facies distribution in boreholes were integrated and adopted as input datasets to compute 3D geometrical models of the fault zone with two

310 different approaches.

A first geometrical model of the selected fault zone has been computed using the 3D geological modelling software Leapfrog GEO (Seequent, Bentley Systems Inc.). Leapfrog GEO is based on implicit modelling methods, using the FastRBF(TM) (Radial Basis Functions) method to interpolate large datasets of sparse points to create continuous meshes with variable geometry. To have a first constraint on the lateral extension and geometry of the selected fault zone(s), a 3D model has been established from

315 tunnel observations and core facies distribution in the cores.

This fault zone model has been used for forward GPR simulation, following the modeling approach of Shakas and Linde (2015) for comparison to the GPR measurements. To account for the slight curvature resulting from the interpolation, the novel meshing approach has been employed, which is introduced in Escallon et al. (2023).

### 5 Multiscale Characterization of Fault Zones in the Rotondo Granite and the Resulting Target Fault Zone

### 320 5.1 Structural Inventory above the Bedretto Tunnel

The results from remote sensing allowed us to identify three main sets of lineaments, showing different orientation, spatial distribution, lateral persistence and relative frequency at the scales of observation (Fig. 3a). These lineament sets include (Fig. 3c-f):

- Set (1) NE-SW to ENE-WSW-striking lineaments, with a lateral persistent of up to several hundreds of meters, organized
325     in a hierarchical spatial distribution, predominant in terms of frequency at the regional scale (lineament lengths 100-1000
    m);

- Set (2) N-S trending lineaments, usually consisting of short segments, with limited lateral persistence;

- Set (3) WNW-ESE to NW-SE trending lineaments, with limited lateral persistence and scattered occurrence in the Rotondo granite.

330

The results from field analyses provided more information on the geological characteristics of the remotely sensed lineaments and allowed us to define a relative chronology between the lineament sets. The deformation sequence inferred from field analyses includes a complex series of brittle, ductile and ductile-to-brittle shear zones that dissect the Rotondo granite. The detailed description of the deformation structures, the deformation sequence, and the related tectonic interpretation is described
335 in a separate paper (Ceccato et al., 2024). Here is a brief summary of the main characteristics relevant to the FEAR project. The sequence (from older to younger) includes three main types of structures (Fig. 3b, g-j):

- Type 1: NE-SW to E-W striking, NW-steeply dipping ductile shear zones with reverse kinematics (Fig. 3h). These shear zones commonly are superimposed on pre-existent magmatic features (mafic and aplitic dykes) and structural discontinuities (shear fractures, cataclasites and breccias) related to the pre-Alpine tectonic evolution of the Rotondo
340     granite (Fig. 4a). The Type 1 structures exhibit a synkinematic mineral paragenesis suggesting amphibolite to upper greenschist facies conditions. The thickness of these shear zones ranges from few millimeters to several meters (Fig. 4b,c). These ductile shear zones are included in lineament Set (1) inferred from remote sensing.

- Type 2: Strike-slip ductile shear zones, mainly ENE-WSW and E-W-striking, overprinting pre-existent ductile shear zones with dominant dextral kinematics (Fig. 3j). Strike-slip shear zones are again included in the Set (1) defined by
345     remote sensing.

- Type 3: These structures are composed of two conjugate sets of steeply dipping, N-S and WNW-ESE-trending brittle-ductile faults with transpressional kinematics inferred from the slightly oblique, shallowly N-plunging lineation. These structures define the lineament Sets (2) and (3) identified by remote sensing. The transpressional faults are usually characterized by chlorite and quartz mineralization in dilational step-overs and tensional veins, suggesting their formation at
350     lower-greenschist facies conditions (e.g., Fig. 4d). In addition, these faults are in some cases related to a local hydrothermal alteration of the granite related to quartz leaching and the development of episyenites, spatially heterogeneous volumes of highly-porous and permeable granite (Pennacchioni et al., 2016).

- Type 4: Brittle fault zones and shear fractures, typically defined by zeolite- and -gouge bearing shear surfaces. Their dominant strike is ENE-WSW-trending, even though reactivation of other minor structures with different orientations
355     is also observed (Fig. 3b,k). These faults mainly localize at the rheological/compositional/mechanical contact between

undeformed host rock and major mylonitic shear zones (Fig. 4b,c-e,f). Therefore, Type 3 structures are included in the lineament Set (1) identified by remote sensing. Zeolite-bearing faults are commonly decorated by thin plane-parallel layers of whitish breccia made of host rock clasts in a zeolite-rich cement. Gouge-bearing faults are characterized by a phyllosilicate-rich gouge layer up to 10 cm in thickness.

360    Multiscale, remote sensing analyses and field investigations of lineament sets and structure types provide fundamental constraints on the spatial organization and geometry, such as lateral extent, of deformation zones. The geometry and spatial organization of Set (1) lineaments and Type 4 brittle fault zones are of particular relevance for the selection of the fault candidate. Set (1) lineaments are the most laterally continuous at the regional scale, composed of both ductile shear zones and localized faults reaching lengths of more than 600 m as continuous planes. The Type 4 brittle faults that define a part of lineament Set

365    (1) are organized in clusters and fault zones at the outcrop scale, with across-strike thicknesses between 2 to 10 m, and lateral persistence of several hundreds of meters (green fractures in Figure 3c). However, these clusters and fault zones are composed of discrete and discontinuous shear surfaces and fracture planes, each of which is usually less than 30 m in length (Fig. 3c). Additionally, Type 4 brittle fault zones exhibit zeolite-bearing shear planes, fault mirrors and cataclasites. Indeed, such zeolite-bearing fault rocks are quite widespread in crystalline basement units of the Alps (Weisenberger and Bucher, 2010),

370    and have been interpreted to likely result from past seismic activity related to (hydrothermal) fluid injection (Dempsey et al., 2014; Ceccato and Pennacchioni, 2018).

## 5.2    Fault Zone Selection

In the process of selection of the candidate fault zones, the southern section of the Bedretto tunnel was excluded, from the entrance at Ronco to TM1100. This section crosscuts the polymetamorphic sequences of the Tremola and Prato series, which

375    are highly anisotropic lithologies where the overburden stress is oblique, making predictions of the stresses acting on the faults highly uncertain, leaving the Rotondo granite section of the Bedretto tunnel. The section extending up TM 1800 was also excluded due to the small rock overburden (< 1000 m), resulting in insufficient stress magnitudes for the FEAR project. Section TM 1800-2000 was excluded as it comprises a highly dissected rock mass, which is hydraulically connected to the neighboring section (TM2000 to TM2100), with ongoing experiments run by other teams at the BULGG. The TM2100-2350

380    section consists of massive Rotondo granite and is devoid of relevant faults. Beyond TM3000 the granite has been deformed into ductile shear zones with a gneissic, anisotropic fabric and lacking evidence of fault reactivation; therefore, structures in this section are considered less favourable. The section between TM 3200 and the connection to the Furka Tunnel was also excluded due to infrastructural and administrative restrictions associated with the borders of cantons Ticino, Wallis, and Uri. Hence, the research was restricted to the section TM2350-TM3000, which includes c.a. 50 potential structures that could

385    roughly correspond to the requirements for the fault reactivation experiments.

Structural mapping revealed a higher density of suitably oriented structures with different degrees of complexity in section TM2350-2550. Detailed scanline surveys (performed at the SW wall; Osten, 2022) indicate multiple overlapping fault zones, clustered in four sets with dip/dip direction of: 53/287 (set 1), 64/319 (set 2), 67/349 (set 3), and 83/88 (set 4). The first
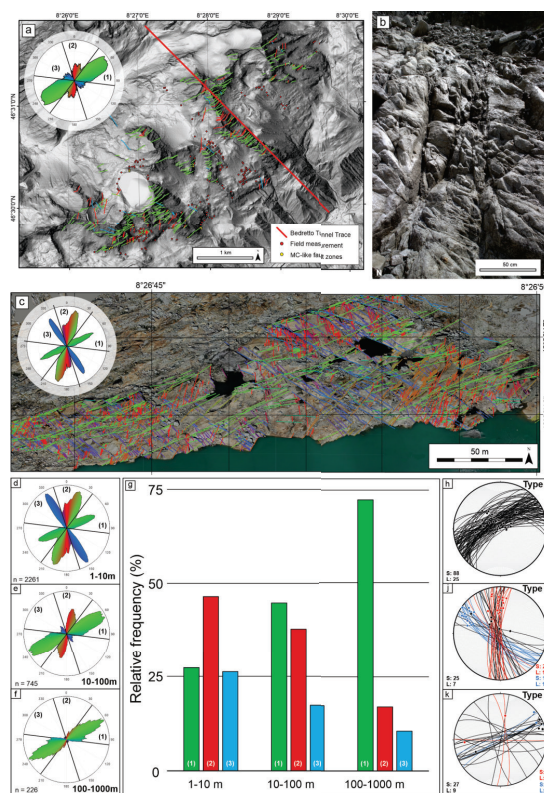
**Figure 3.** Summary figure presenting the preliminary results of the remote sensing data and field survey in the Rotondo granite area. (a) DTM of the Rotondo granite area showing the trace of the Bedretto Tunnel relative to the investigated points on the surface (red dots). Field occurrences of MC-like fault zones are represented by yellow dots. The lineaments interpreted from remote sensing are color coded according to their strike (Hillshaded DEM from SwissALTI3D). (b) Field example of MC-like fault zones, represented by a narrow fracture corridor with multiple principal slip planes. (c) Interpreted outcrop map with the traced lineament. Ortho-images obtained from drone surveys. (d-f) Rose diagrams obtained from the analyses of the lineament length data obtained from remote sensing, showing the distribution of lineament strike for each length class (c: 1-10 m; d: 11-100 m; e: 101-1000 m). (g) Histogram showing the relative frequency of the lineament sets (1-3) identified by remote sensing at each resolution scale. (g-j) Equal area, lower-hemisphere stereographic projections of the structural inventory from field analyses. Great circles: slip planes (S); Dots and contour: lineations (L). Blue and red planes and dots represent dextral and sinistral kinematics, respectively. Data from Ceccato et al. (2024). (h) Type 1 ductile shear zones. (j) Type 2 brittle-ductile faults. (k) Type 3 Zeolite- and gouge-bearing brittle fault zones.
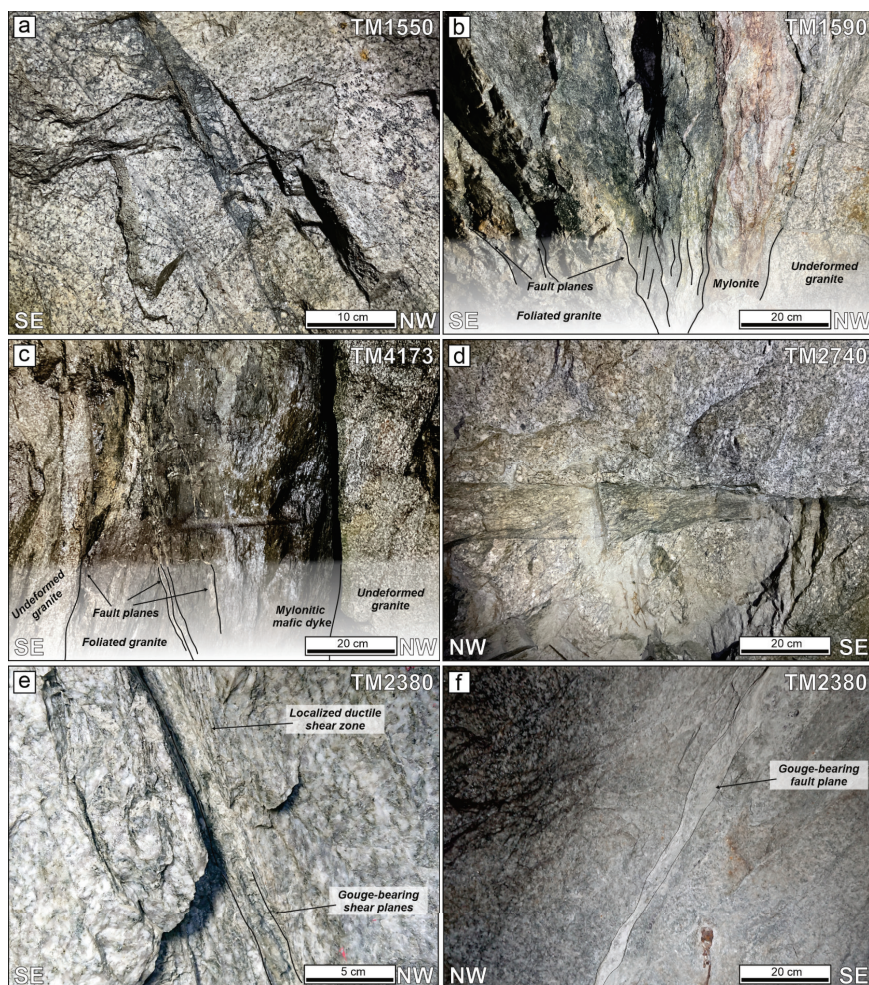
**Figure 4.** Types of deformation zones observed in the Bedretto Tunnel. (a) Brittle breccia formed during pre-Alpine formation ($D_1$ brittle cataclasite described in Ceccato et al. (2024). (b-c) Type 1 ductile shear zone localized on pre-existent compositional and structural discontinuities. Note the occurrence of late-stage Type 3 fault planes. (d) Type 2 brittle-ductile faults. (e-f) Type 3 zeolite- and gouge bearing brittle faults. These pictures represent the fault planes at the MC fault zone outcrop.

two sets can be grouped into a single set with average orientation of 58/303. Fault zones oriented sub-parallel to the tunnel

390    (striking NW-SE) were excluded due to the difficulty in resolving their positions and geometries and the risk posed to existing

infrastructure in case of reactivation.

The estimated stress components in the BULGG, based on mini-frac tests in boreholes at TM 1750-2250, are SHmax = 25.4 ± 2.3 MPa, and Shmin = 14.6 ± 1.4 MPa (Bröker and Ma, 2022). The average vertical stress Sv, calculated assuming an overburden of 1000-1100 m with a constant rock density of 2.62 g/cm$^3$, is 26.5 MPa. SHmax direction is approximately N100E
395  (Ma et al., 2022), albeit with some variations. Thus, fault zones that exhibit steep to intermediate dips and strike orientation between NE-SW and NW-SE yield the highest slip tendency (up to 0.4, Ma et al., 2022) and have been selected as primary subjects of investigation. It is worth noting that the absolute values of slip tendency are lower than the empirical Byerlee's friction values ($\geq$ 0.6) expected for granite, and possible stress variations near the fault zone have been observed (Zhang et al., 2023), which could modify the slip tendency significantly. Determined by He-pycnometry and water saturation methods, drill
400  core samples from fault zones yielded a density of around 2.6 g/cm$^3$, and total and connected porosity of 1.9-2.8 % and 0.9-1.1 %, respectively (Osten et al., 2024). These properties varied little across fault zones.

GPR measurements conducted along the tunnel walls, between TM 2350 and TM 3200, indicate clear reflectors as lines sub-parallel to the tunnel. This is a result of the acquisition geometry of the GPR system, which is primarily sensitive to reflectors along the direction of travel, as seen in Fig. 5. While the entire section has been scanned on both sides, it has been observed that
405  the section from TM2750-3200 corresponds to a significant water-bearing, interconnected "reservoir". This observation agrees with consistent compositions and similar physico-chemical properties of fluids measured across this section (Arnet, 2022). However, lower temperatures with a higher pH and low mineralization have been measured in larger fault zones, partially resembling the meteoric or glacial surface water (Arnet, 2022). Notably, the transition in water chemistry, GPR reflections and anisotropic rock fabric corresponds to the change from equigranular Rotondo granite (RG1) to the porphyritic Rotondo granite
410  (RG2). Considering these results, we further restricted our assessment to the tunnel section around TM 2350 to TM 2750 for the selection of the candidate fault zone.

Roughly 5-7 MPa of water pressure have been measured in the exploration boreholes some 15 m from the tunnel wall, agreeing with previous measurements in boreholes around TM 2050 in about 100-200 m below the tunnel floor (Ma et al., 2022) and at the junction to the Furka Basetunnel (Ofterdinger et al., 2014; Lützenkirchen and Loew, 2011). These head measurements
415  indicate an almost horizontal head distribution in the overburden ranging from 800-1300 m across the mountain ridge. Thus, the rock mass is under-pressurized, which potentially is a result from the long lasting drainage of the tunnel. Permeability, as determined using a) unconfined gas permeameter measurements on cores, b) flow through cells on confined core samples, and c) hydraulic testing in various boreholes varies between E-20 and E-13 m$^2$ in close proximity. Fluid flow is strongly focused onto single open or partially mineralized fractures with permeability of E-13 to E-16 m$^2$ (Osten et al., 2024). As observed from
420  tunnel inflows and borehole flow logs the main flow paths are along the bounding faults which are partially well connected through the more fractured rock-mass in between. Average protolith permeability range between E-18 to E-19 m$^2$ (Osten et al., 2024; Braun, 2023).
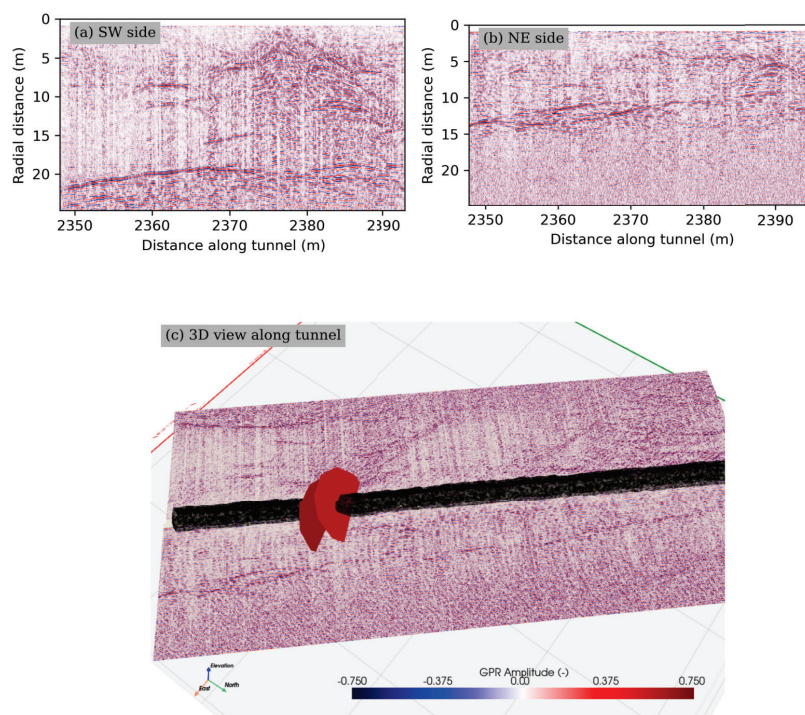
**Figure 5.** Directional GPR scans along the a) SW side of the Bedretto Tunnel around the MC FZ (TM2345-2395); b) NE side of the Bedretto Tunnel around the MC FZ (TM2345-2395); c) Oriented 3D view of the GPR sections with the orientation of the MC FZ

### 5.3    Fault Zone Characterization

The constraints from analyses in the tunnel reduced the selection to a total of five candidate structures with a good fit to the ideal characteristics for the FEAR project (see Section 3). The relevant properties of the remaining five fault zones are briefly described in comparison to the ideal fault zone for the FEAR planned experiments in Table 1. As shown in the compilation, the fault zone at TM2380-2390 is slightly more suitable than the other structures. This structure is further termed MC fault zone. The MC fault zone is located at TM2380-2390, and the GPR reflections on either side of the tunnel reveal that this fault should extends more than 15 m beyond the tunnel walls and into the rock volume (Fig. 5c). The reflections are more intensely observable at the South-East wall of the tunnel (Fig. 5a). The MC fault zone is located in a section of RG1 granite showing few

**Table 1.** Selection criteria applied to candidates.

| Candidate# (after Jordan, 2019) | Ideal | MC (#+48/+48.1/+49) | +57.2 | DG (#+68) | FA (#+71/+72/+73) | +75.1&2 |
|---|---|---|---|---|---|---|
| TM | - | 2380-2390 | 2430-2440 | 2489-2524 | 2578-2590 | 2600 |
| *Damage zone thickness/extent* | 1-10 m | 6 m | 2 m | 5 m | 7-10 m | >7 m |
| *Fault core thickness/extent* | abundant | 3x<0.1 m | <0.05 m | 2x<0.1 m | 3x<0.1 m | unclear |
| *Planarity/curvature* | planar | planar | planar | offsets possible | planar | planar |
| *Fault intersections/ connectivity to nearby faults* | no intersections | NW-SE W-E | all sets | all sets | NW-SE N-S | NW-SE N-S W-E |
| *Vertical and horizontal extent* | >50 m | >40 m | uncertain likely>30 m | >90 m | uncertain likely >50 m | >60m |
| *In between two favorable faults?* | yes | yes | yes | yes | yes | yes |
| *Permeable* | wet to heavily dripping | heavily dripping | dry-wet | small inflow | heavily dripping | wet |
| *hydraulic connectivity with surrounding rock mass* | no connection | loose network | SW: dense network NE: loose network | dense network | loose network | SW: no network NE: loose network |
| *hydraulic connectivity with surface or bottom?* | connection to surface | likely | likely | likely | likely | likely |
| *Gouge* | yes | yes | yes | yes | yes | unclear |
| *favorable coating?* | yes | yes | yes | yes | yes | yes |
| *homogeneity/isoptropy in the rock mass* | homogeneous/ isotropic | small shear zone? | homogeneous/ isotropic | highly anisotropic/ asymmetrical | homogeneous/ isotropic asymmetric? | unclear |
| *Orientation (dip/dip direction)* | - | 42-68/305-318 | 61-64/351-359 | 43-56/17-23 | 54-73/356-10 | 62-76/230-237 |
| *proximity to failure* | >0.6 | 0.24-0.28 | 0.31 | ~0.3 | 0.26-0.31 | 0.27 |
| *representative fault trending* | NE-SW | NE-SW | W-E | none | W-E | NW-SE |
| *favorable dip in normal-faulting or strike-slip faulting environment* | both | both | both | NF | both | both |
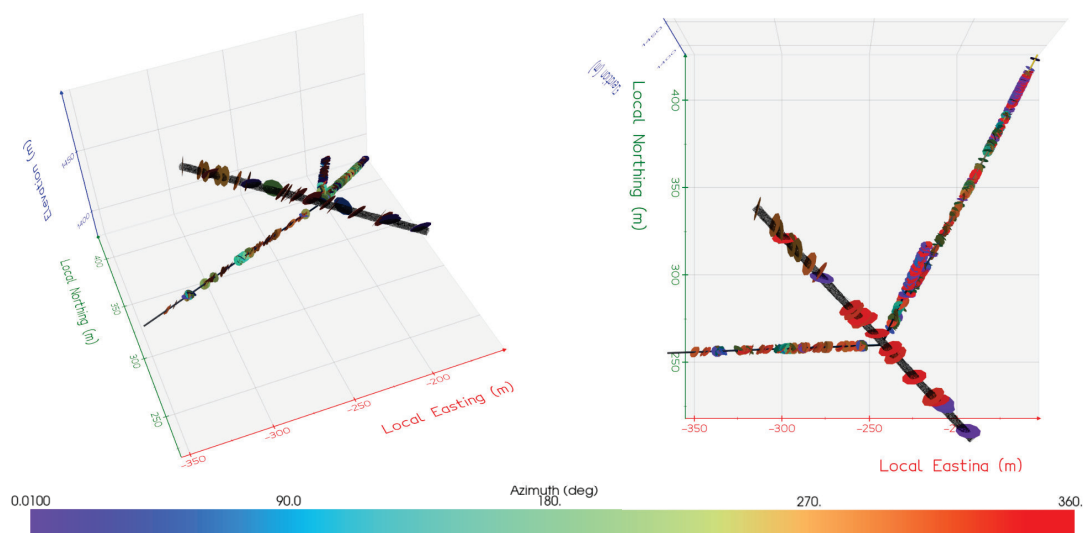
**Figure 6.** Structures (both faults and fractures) observed along the tunnel and boreholes in the vicinity of the FEAR experimental volume, with an extent of roughly 250 m³. To highlight their orientation, we plot the structures colored according to their azimuth.

and small deformation structures. The MC fault zone belongs to the Type 4 structure set (Section 5.1), its overall orientation is 65/330 and the lateral persistence of this fault zone is likely to exceed 100 m, as inferred from the analysis of surface lineaments with compatible orientation (Type(4)-Set (1) lineaments, Fig. 3). On the tunnel wall, the fault zone is composed of a set of shear fractures bounded by two discrete main shear planes (labelled F#+48 and F#+49 in Fig. 7), sandwiching a roughly 2-7 m wide

435 zone of higher fracture density compared to the intact Rotondo granite. Roughly in the center, another main central shear plane was observed (labelled F#+48.1 in Fig. 7), which is decorated by a gouge layer.

Each main shear plane (F#+48, 48.1, 49) is localized on a pre-existent 5-10-cm thick ductile shear zone defined by a biotite-rich foliation and weak lineation (Fig. 4e-f). Overall, the lineations on the shear planes of the MC fault zone show a wide range of orientations, suggesting a long-lasting multi-mode history of movement, dominated by reverse (compressive) to strike-slip

440 shear senses, as inferred from meso-structural kinematic indicators showing a SE-ward shear movement. The MC fault zone contains several other discrete fracture planes that differ in strike by 20-30°compared to the shear planes bounding the fault zone. The central main shear plane (labelled F#+48.1; Figs. 7a, 4f) is oriented 58/318. The fault rocks observed along the main shear plane are composed of a zeolite-rich cemented cataclasite/breccia (< 50 mm, Fig. 4f) that features a thin (< 10 mm) gouge layer, with a patchy, discontinuous distribution on the shear plane. The gouge composition is very close to that of

445 the host granite, with a slight enrichment in phyllosilicates, mainly muscovite and minor chlorite (for detailed description and illustration we refer to Volpe et al., 2023). Laboratory shear experiments were performed on the gouge from the MC fault zone

to simulate in-situ stresses and fluid pressures (Volpe et al., 2023). The analysed gouge is overall slightly velocity strengthening but it was demonstrated that it still can slip seismically if the hydraulic pressure is sufficiently large (Volpe et al., 2023).

### 5.4 Borehole Investigation of the Target Fault Zone

450 To gain insights on the lateral continuity of the MC fault zone and its geometry, data from borehole logging, cores, and GPR imaging has been integrated into a 3D geological-geometrical model as explained below.

#### 5.4.1 Borehole Logs, Cores and Facies Description

In order to identify the occurrence of the MC fault zone at depth along the boreholes, rock cores from BFE_A05, _A06, _A07 were analyzed and classified in different Core Facies, representing segments of the cores with similar geological characteristics.

455 Comparing the Core Facies to the characteristics of the MC fault along the tunnel wall, and defining the position of the different Core Facies along the boreholes we constrained the overall geometry and occurrence of the MC fault at depth.

The Core Facies adopted for the classification of the cores include (Fig. 8):

- F0: intact rock with rare (« 5/m) thin and cohesive fractures filled with phyllosilicates.

- F1: facies characterized by a dense set of oriented cohesive fractures filled with phyllosilicates, and with mylonitic fabric.

460 - F2: similar to F1, but fractures are not cohesive; the granite is characterized by enhanced porosity and incipient (hydrothermal) alteration.

- F3: severely damaged rocks with oriented fractures and presence of cataclastic breccia or fine gouge. The gouge is usually accidentally removed during core extraction, but small patches persist on some fractures.

- F4: cataclasites/ heavily fractured granite cemented by zeolites with high matrix porosity (rare).

465 Each facies is characterized by different petrophysical (permeability) and mechanical (cohesion) properties, which are briefly summarized in Fig. 8b. The analysis allowed to define the position of the MC fault zone at depth along the boreholes. that in particular, core facies F3 resembles the main plane F#+48.1 with a higher density of open fractures, the occurrence of loose gouge material and minor hydrothermal alteration seen as porous granite. Accordingly, BFE_A05 and BFE_A06 intersect the MC fault zone at 37-45 m (Fig. 8c) and 22-27 m from the tunnel wall, respectively. BFE_A07 crosscuts only a thinner and less

470 developed (minor brittle damage) part of the fault zone at 71-72 m (Fig. 8d).

Optical and Acoustic televiewer (OTV, ATV) logs confirm the observations independently, adding orientation information for the fractures. Five clusters have been identified in the MC borehole sections resembling the MC fault zone: 71/350 (strike 80°), 63/350 (strike 80°), 58/38 (strike 128°), 66/237 (strike 147°), and 59/300 (strike 30°) with consistently open fractures (Fig. 8d,10a). The orientation of the fractures associated with the MC fault zone at the tunnel wall is more variable but consistent

475 with the observations from the boreholes (Fig. 10a).
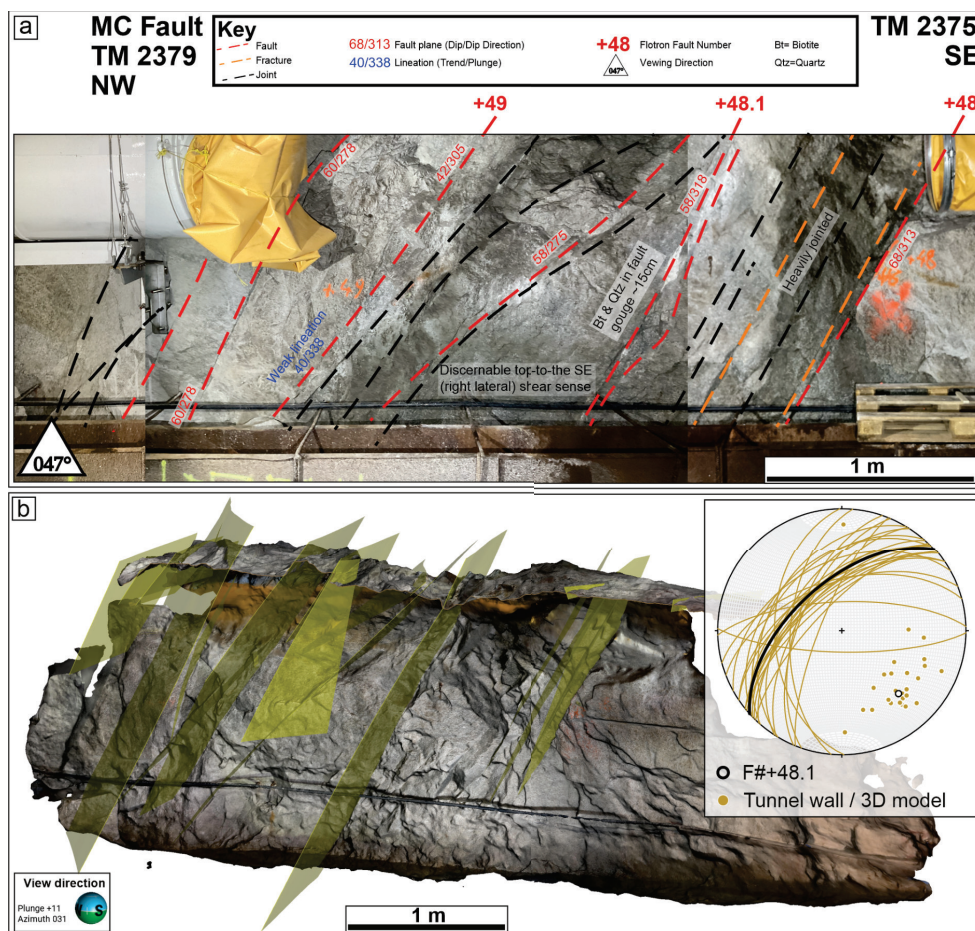
**Figure 7.** The MC fault zone in the tunnel, rock cores and boreholes. (a) Structural interpretation of the exposure of the MC fault zone along the NE wall of the Bedretto Tunnel at TM 2380. (b) 3D model of the NE tunnel wall around the MC fault zone at TM2380. The yellow transparent planes represent the fracture planes interpolated from manual fitting in Leapfrog GEO. The stereoplot in the upper right inset reports the orientation (great circles and poles to planes) of the observed and modelled fracture planes, including: F#+48.1 on the tunnel wall; Orientation of the fractures inferred from analysis of the 3D model of the tunnel wall.
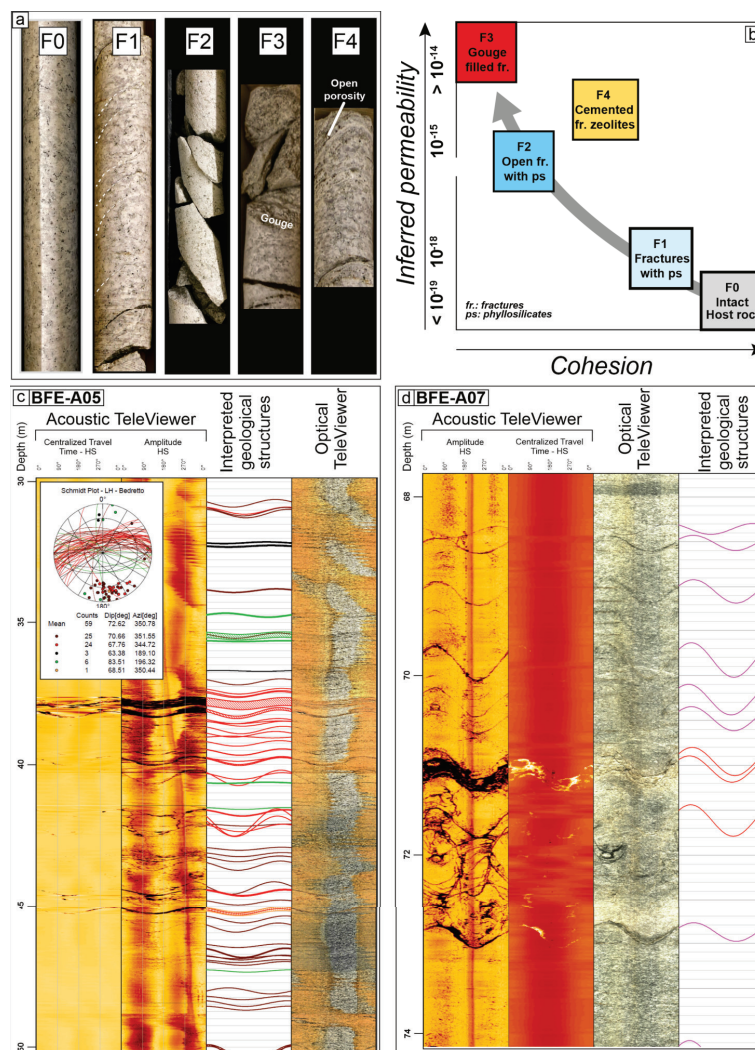
**Figure 8.** (a) Examples of segments of rock cores extracted from the BFE-boreholes representing the different core facies. (b) Qualitative diagram describing the relationship between core facies numbering, cohesion level of the rock core and the inferred permeability. (c-d) Example of integrated logging of borehole (BFE_A05, 30 to 50 m depth; BFE_A07, 68 to 74 m depth) from Acoustic (ATV) and Optical (OTV) televiewers with the associated orientation of the interpreted geological structures plotted in the inset stereoplot.

### 5.4.2   Single-Hole GPR-Imaging

Single-hole GPR measurements were collected along each of the BFE-boreholes (Fig. 9. The radargrams yield with the 20 MHz antennas are presented and interpreted, showing the MC fault zone clearly. The GPR reflections generated from the MC fault zone are evident in all three boreholes and reach more than 100 m laterally into the adjacent rock mass. The possible tunnel

480    intersection of these reflectors are consistent with those of the main planar features measured in the tunnel. Nevertheless, the azimuthal ambiguity prevents delineation of the exact origin of the reflections. Along the radargrams, the boundaries of the MC fault zone have been delineated by V-shaped (chevron) patterns, which result from the intersection of faults and boreholes at a high angle (Olsson et al., 1992). The reflectors intersect the boreholes at the depths where the interpretation of the core and wireline logs suggest the presence of the fault zone. The rock mass between the two to three main reflectors appears as a

485    high-contrast zone suggesting the presence of a water-filled fracture network. The GPR in BFE_A05 additionally shows that the MC fault zone crosses a  20 m wide, W-E striking shear zone (called DG or FZ#+68).
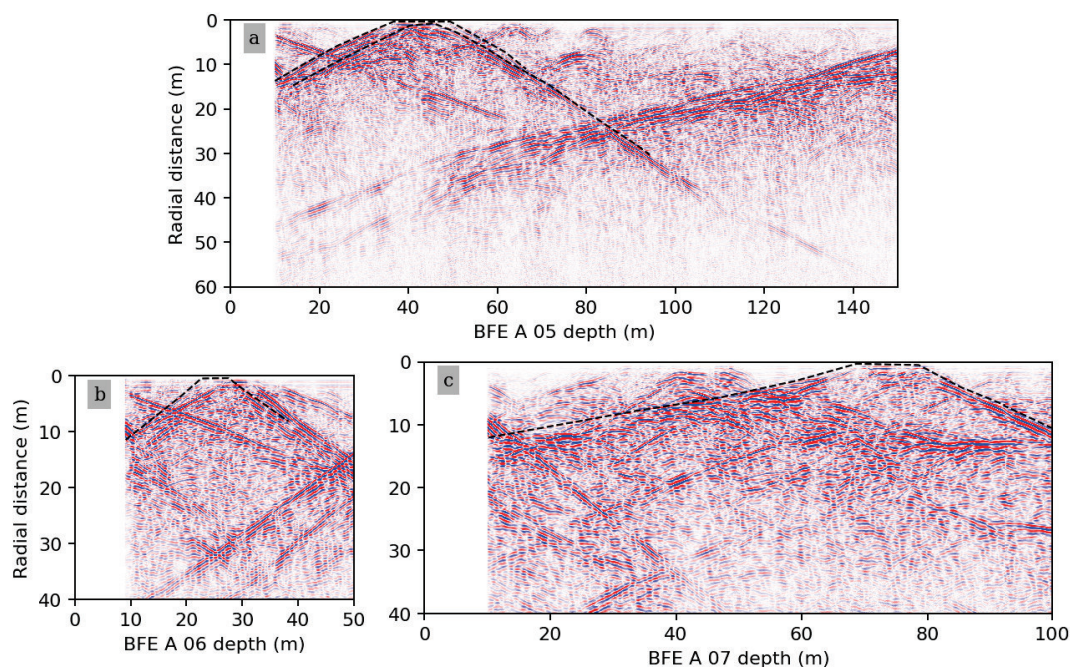
**Figure 9.** GPR profiles along the exploration boreholes with trace of the MC FZ indicated a) BFE_A_05; b) BFE_A_06; c) BFE_A_07.

### 5.5 3D Geometrical Model of the MC Fault Zone

The model of the MC fault zone (Fig. 10a-c) resulting from the field investigation consists of two main bounding faults. These two planes crosscut the tunnel at the approx. location of F#49 and F#48 at the wall. The planes have slightly different

490 orientations but converge towards the SW side of the tunnel (Fig. 10b). These two bounding planes boarder a roughly 2-7 m wide zone of higher fracture density compared to the intact Rotondo granite (Figs. 8a, 10a). This model is supported by the fracture intensity distribution along the boreholes and the analyses of similar structures at the surface, which suggests that the fault zone presents a laterally variable fracture intensity (Figs. 3c, 10d).

Tunnel wall mapping, borehole and core logging, and GPR profiles support the interpretation that the MC fault zone is a

495 laterally continuous deformation zone over more than 100 m, extending at least from the intersection of BFE_A07 in the west to the intersection with the DG/F#+68 fault zone in the east (Fig. 10b). Similarly to the Set (1) - Type 3 structures identified by field and remote sensing analyses (Figs. 3b, 10d), the MC fault zone is probably composed of anastomosing fault and fracture planes (< 30 m in length), with 20-30 °strike variability.

### 5.6 3D GPR Simulation

500 To further examine the consistency and validity of the proposed 3D geometry for the MC fault zone, we performed forward simulations of the GPR response in 3D, using the method described in Shakas and Linde (2015). The synthetic GPR response has been simulated based on a fractured volume bound by two faults in a volume of intact Rotondo granite with a source that is representative of the transmitter similar to that used in the field. The aim has been to test whether the proposed geometry is corroborated by the GPR data, but not to further adjust the geometry and seek a "best-fitting" response. The results of

505 the simulation are shown in Fig. 11. The resulting two V-shaped synthetic GPR reflectors are plotted against the radargrams measured in the boreholes penetrating the MC fault zone (see Fig. 9). Overall, the field and synthetic data agree in both shape and extent for the continuity of the MC fault zone. Some discrepancies occur, as for example the mismatch in radial distance of the MC FZ from the BFE_07 borehole, notably in the first 60 m. Causes for this discrepancy may be multifold, including deviations of the fault geometry from a plane, minor corrections in the velocity model used to convert travel time to distance,

510 or simply an inability of the simplified geometry and forward solver to capture the true nature of the complex fault zone. In future work, we will focus on addressing these topics individually.

## 6 Discussion

Site investigations often focus on assessing rock masses for construction or excavation, where fault zones pose significant hazards (e.g. Hunt, 2005 Fookes et al., 2015). Similar studies are conducted for siting underground laboratories like GeoLab

515 and Bukov Underground Lab (Schill et al., 2016; Bukovská et al., 2019) or smaller-scale experiments in other underground facilities (e.g. Amann et al., 2018). However, identifying a single structure within a tunnel for a large-scale experiment demands a comprehensive, constraint-driven approach, as described here. To pinpoint the ideal site amidst the complexities, the
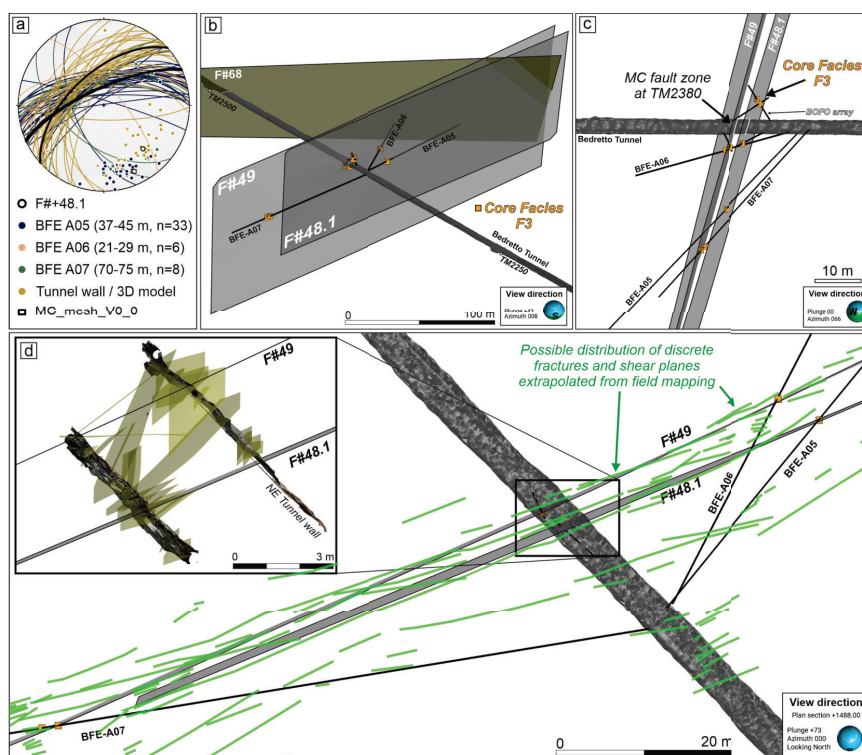
**Figure 10.** 3D Geometrical model of the MC fault zone from tunnel observation, core facies distribution, and borehole logging. (a) 3D model of the NE tunnel wall around the MC fault zone at TM2380. The yellow transparent planes represent the fracture planes interpolated from manual fitting in Leapfrog GEO. The stereoplot in the upper right inset reports the orientation (great circles and poles to planes) of the observed and modelled fracture planes, including: F#+48.1 on the tunnel wall; orientation of the fractures in BFE-boreholes as inferred from OTV/ATV logging; Orientation of the fractures inferred from analysis of the 3D model of the tunnel wall; orientation of the two main meshes (MC_mesh_V0_0) defined through interpolation of tunnel, core and borehole data. (b) Overview of the 3D model of the MC fault zone, composed of two main surfaces (meshes F#+49 and F#+48.1 bounding a zone of high fracture intensity. (c) Side view of the 3D model showing the distribution of the borehole arrays and the location of the F3 facies in each borehole. (d) Plan view of the MC fault zone showing the two main surfaces interpolated from core facies distribution. The light green traces represent the likely heterogeneous distribution of discrete fractures and shear planes as inferred from field mapping of structures similar to the MC fault (Fig. 3c). The inset shows the fractures interpreted from LiDAR scanning and structural analysis of the tunnel wall. Note the slight difference in orientation between the tunnel wall fractures and the interpolated surfaces.
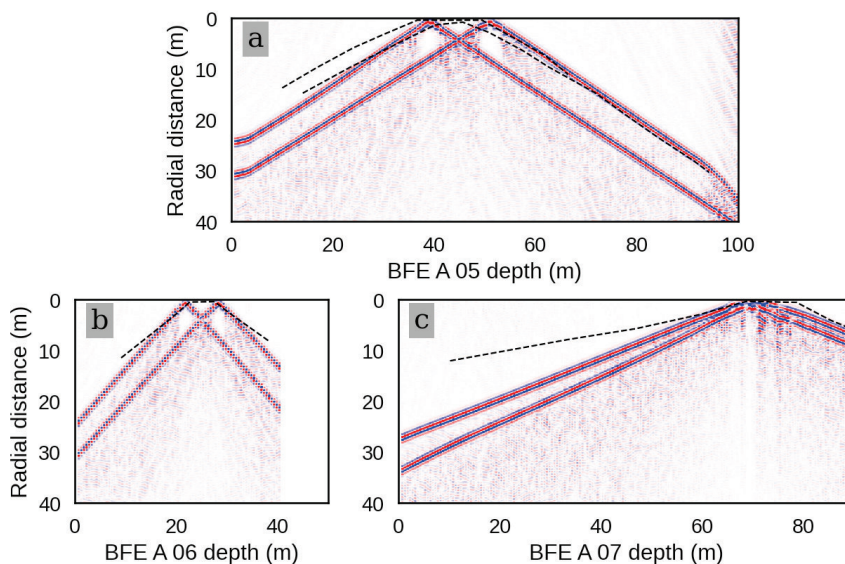
**Figure 11.** GPR forward model using the methodology from Shakas and Linde (2015) and the 3D geometry for the MC fault zone, both planes 48 and 49. The simulation aimed to reproduce the results observed in borehole BFE_A_05. The (dashed) line superimposed on the image is the trace of the MC FZ picked from field observations (see Fig. 9).

structural inventory of the Rotondo granite was systematically narrowed down to the MC fault zone. Alongside conventional site selection methods such as legacy data screening, remote sensing, and field mapping, unconventional techniques like tunnel

520 inflow evaluation and Ground Penetrating Radar (GPR) were used to meet the specific data requirements. A similar constraint-based approach was employed in siting the EGS-Collab-Hydroshear-Experiment 2 (Dobson et al., 2018), albeit with limitations primarily involving invasive geometrical fracture analysis and logistical considerations. Despite the specific and stringent constraints imposed by FEAR's scientific goals and experimental design, this approach holds promise for other projects where identifying fault zones is critical, such as siting disposal chambers in underground nuclear waste facilities or locating prospec-

525 tive fault zones around hydrothermal exploration boreholes.

The selection of the fault zone marks a pivotal milestone for the FEAR project. Identifying the target fault zone is crucial for achieving FEAR's objectives and implementing experimental designs. This is particularly vital for developing the Bedretto on-fault observation system (BOFO) by deploying a dense monitoring network comprising seismic, pore pressure, stress, and strain sensors. The selection process relies on geological, geometrical, hydraulic, and geomechanical constraints of the faults

530 and host rocks, further characterizing each fault zone in terms of architecture, geometry, and complexity. Employing a multidisciplinary approach is essential to manage the heterogeneity and complexity of natural fault zones. The insights gained

inform the experimental design and the excavation of the 125-meter-long experimental tunnel, finalizing the configuration of the BOFO. Information on the target fault zone will be refined during and after each FEAR stimulation experiment, progressively enhancing understanding of inferred heterogeneity and complexity.

535 The FEAR stimulation experiments will differ from existing underground experiments because fluids will be injected into a well-identified fault zone and not into an otherwise undefined fractured rock volume. Furthermore, the FEAR objectives go beyond the generation of induced seismicity in a selected fault zone. FEAR aims to induce fault motion and seismicity on a pre-conditioned fault zone. This implies that the stress state and pore-pressure conditions of the target fault zone will to a certain extent be constrained and continuously monitored during the experiments. The multidisciplinary approach to fault zone 540 selection and characterization presented in this paper will be essential to interpreting the stimulation experiments and their response to heterogeneity in rheological, frictional, hydraulic and poro-elastic parameters that define the target rock volume.

As indicated by e MC fault zone meets several of the geological-geometrical criteria put forth for the FEAR project in section 3. The b___ fault system described here for the MC fault zone consists of a fractured rock mass, in which fractures and shear planes localized along ductile precursors, locally associated to hydrothermal alteration (e.g., episyenites). Similar 545 brittle shear zones derived from ductile precursors have been investigated within the framework of the exploration of basement geothermal systems. In the following, the geological character of the MC fault zone is compared to a few selected case studies, e.g. Karelia region (Finland), Soultz-sous-Forêts (France), Basel and Aar massif (both Switzerland), in order to retrieve preliminary constraints on the (induced) seismic behavior of the fault zone.

– Fault zone structure and dimension

550 The MC fault zone is relatively simple from a structural geology perspective as it is immature, with an absence of gradual transition from core to wall zones. Indeed, the principal fault planes are likely not developed by progressive shear localization (sensu Faulkner et al., 2010) by cataclastic means, but rather by preferential splitting and limited dislocation along pre-existing anisotropies (e.g., hydrothermal breccias and mylonitic foliation). It consists of a 2-7 m wide fracture corridor (fracture density < 30 m$^{-1}$), which is bound by two main fault planes from the protolith, and presents a thin 555 cataclastic zone (<5 cm thick) in a third plane localized between the previous two, here referred to as "fault core". Thus, the MC fault zone is a rather thin structure, composed of an immature fault core and less-developed "damage zone" when compared to the other case studies. Additionally, the fracture density within the fracture zone appears asymmetric; outside the bounding faults the fracture density declines to background values within a short distance. Although, the width of the stimulated fault zones in the Soult-sous-Forêts granite is in the order of 10 m, the fault zone structure is 560 much more complex, including several well-developed cataclastic fault cores (each of which several tens of cm wide) surrounded by hydrothermally altered granite (e.g., Evans et al., 2005). These fault zones belong to a set of regional structures persistent over several kilometers along strike. A similar geological situation occurs in the Basel 1 EGS site, in which the induced seismicity localized along a major, regional-scale fault zone in a similar granitic basement unit (Häring et al., 2008). In both cases, the described fault zones were capable of hosting micro-seismic events with moment 565 magnitude between -1 and 3 (e.g., Evans et al., 2005; Häring et al., 2008).

In contrast, the faults and shear zones stimulated during the injection experiments at Grimsel Test Site (GTS, Aar massif)

are comparable in terms of dimension and geological evolution to the MC fault zone (e.g., Krietsch et al., 2020b). Still, the shear zones in GTS present a pervasive ductile fabric over a thick (20-50 cm) volume of rock, and are continuous over very long distances (> 500 m). During stimulation at the GTS, the maximum observed moment magnitude of

570    induced seismicity was in the order of -2 to -3 (e.g., Gischig et al., 2019). Both brittle fault zones and shear zones in the Rotondo granite grow by linking disconnected segments of pre-existing structural discontinuities (Ceccato et al., 2024). The potential curvature and the roughness of the fault zone is thus a result of the complex sequence of reactivation of structures through the brittle-ductile-brittle tectonic evolution of the Rotondo granite. The MC fault zone is composed of multiple segments of finite (maximum  30-50 m) length aligned over large distances, and it is therefore theoretically

575    capable of hosting seismic events of the same magnitude, if not higher (depending on the injection procedures) than the GTS induced seismicity (e.g., Gischig et al., 2019).

– Porosity and permeability

Another important geological characteristics is the occurrence and distribution of permeable fluid pathways in the fault zone. In the previous reported case studies, the porosity/permeability is mainly controlled by pervasive alteration of the

580    granite (e.g., Evans et al., 2005; Ledésert et al., 2010). Recently, Bischoff et al. (2024) investigated a hydrothermally altered brittle shear zone along roughly 10-20 m normal thickness indicated by higher fracture intensity in monzonite and granite, showing a complex architecture with porous, multiple fault cores, composed of breccia and altered fault rocks, adjacent to impermeable ultramafic intrusions (compare Fig. 7 in Bischoff et al., 2024). Lenses of variably damaged and altered rock are incorporated into the shear zone. The breccia and the altered core sections show increased effective

585    porosities of up to 18% in comparison to the intact rock mass, which has a density of  2.6 $g/cm^3$ and porosity of 0.4-1.3% similar to the Rotondo granite RG1 around MC fault zone (David et al., 2020; Osten et al., 2024).

The yielded permeability of the MC fault zone is comparable to the measurements by Bischoff et al. (2024) for 1 MPa confinement, ranging around E-18 $m^2$ for micro-fractured granite, fractured granite between E-12 to E-15 $m^2$, and hydrothermally altered granite up to E-14 $m^2$ (Osten et al., 2024) for unconfined gas permeameter measurements. Although

590    hydrothermal alteration has been observed in cores drilled through the MC fault zone, which has some contribution to the hydraulic behavior at large, the spatial distribution of the phenomenon along fault remains unknown. Similar to the observations at the MC fault zone, bounding faults showing increased water flow (Cheng and Renner, 2017) and more than 20% of porosity (Caspari et al., 2020) have been reported from a hydro-geophysical analysis of a borehole penetrating a brittle shear zone in the Aar-massif (Grimsel Pass, Switzerland). At higher pressures however, open fracture permeability

595    has been observed to break down to E-20 to E-16 $m^2$ at 20 to 50 MPa confining pressure (Bischoff et al., 2024). Hydrothermally altered granite almost remains unaffected with increasing confinement (Bischoff et al., 2024). Nonetheless, the local permeability at the selected experimental patches likely will be controlled by the discrete shear planes bounding the MC fault zone and cross connections between them. Their geometry and distribution is quantitatively constrained by the geophysical interpretations, leading to a much more predictable hydraulic behavior.

600      – Isotropic host rock

The host rock surrounding the MC fault zone is characterized by the absence of pervasive ductile fabrics, as observed in many of the other case studies (e.g., Krietsch et al., 2020b). The isotropic host rock relates to predictable elastic (and petrophysical) properties, which leaves the seismic response of the host rock unaffected and eases the seismological analyses of the induced seismic events (e.g., Gischig et al., 2019; Wenning et al., 2018).

605      The characteristics of the MC fault zone are similar to the ones of faults zone encountered in most of the crystalline environments with similar mineralogical composition and resulting similar distribution of physical properties. Therefore the MC fault zone can be considered representative of such crystalline environments and the results of the FEAR experiments will be transferable to other regions in the world, may it be for the analysis of induced or natural seismicity. However, some of the properties are indicated as non-ideal, which impact is discussed below.

610      – Challenges for FEAR

Despite the rather simple structural composition, the MC fault zone proves to be still complex from the perspective of the FEAR experiments as it is a composite structure (several fault planes) with potential interaction at intersections with other fault zones such as with the DG fault zone. This poses some challenges for the experiments, mainly for 1) fault zone characterization (stress and permeability distribution), 2) flow path prediction and development (e.g. hydraulic short-

615      circuits), 3) density of the monitoring network and 4) increased complexity of computational modelling approaches. The controlling factors for triggering small earthquakes with high-pressure fluid injections are flow path distribution and pressure evolution within the fault zone in space and time. Intense hydraulic characterization methods facilitate the development of high-resolution hydraulic and flow models valid for relatively low pressures. As shown by Krietsch et al. (2020b), high-pressure injection may cause new or changing flow path during an injection. This complex interaction

620      of the characterization and the fault zones architecture affects the in-situ characterization phase, and raises the risk of an ambiguous determination of stress and hydraulic characteristics based on packer testing. This challenge increases proportional with the fault zone complexity. At the same time, smaller scale complexity ("fault roughness") stemming from fault zone intersections are points of earthquake nucleation and earthquake arrest avoiding runaway-seismic events. The inferred characteristics of the fault zone serve as key input properties for numerical simulations needed for designing

625      the sensor network geometry and the stimulation strategy. To mitigate these risks, we have integrated a variety of geo-mechanical data, the complexity of faults zone, the associated experimental uncertainties in our approach to identify the target fault zone. Still, the monitoring setup (i.e. special and temporal resolution) and characterization strategy must account for the anticipated experimental complexity and must be adopted along the experimental sequence accordingly.

## 7   Concluding Remarks

630   In the framework of the Fault Activation and Earthquake Rupture (FEAR) project, a densely instrumented fault zone will be repeatedly activated ~~and~~ controlled by hydraulic simulations, aiming at generating earthquakes up to magnitude 1. The design and execution of experiments require the detailed knowledge of several site properties, such as rock mass characteristics, size,

persistence and architecture of the target fault zone, the petrophysical and seismo-hydro-mechanical properties, the stress state as well as the monitoring infrastructure.

635   In this paper we have discussed the selection process of the target fault zone, starting from the experimental goals and associated requirements; presenting and interpreting available data to restrict the search perimeter. Subsequently, a single structure has been selected based on an interdisciplinary, multi-scale and multi-method campaign conducted in the Rotondo granite, consisting of structural geology field work on the surface and in the sub-surface, near- and far-field remote sensing, geophysical investigations along the Bedretto tunnel and in boreholes, borehole logging, mineralogical and petrological analysis, field-

640   and lab-based rock mass and structural characterizations. We further corroborated the fault's continuity into the rock volume by performing ground penetrating radar forward simulations on the 3D geometry of the MC fault zone.

The chosen structure is described as a several meters wide brittle overprinted shear zone, consisting of an fractured volume sandwiched by two or more main fault planes, persistent over more than 100 m. It consists of multiple interlinked planes along strike. The structure is steeply NNW-dipping and thus, preferentially oriented for slip in the regional stress field.

645   The results are already confirmed by the establishment of the Bedretto-On-Fault-Observatory (BOFO) in short boreholes drilled from the Bedretto tunnel through the MC fault zone. To further facilitate close-range instrumentation, a tunnel up to 125 m long has been designed, parallel to the MC fault zone. The final decision on the trajectory of the tunnel parallel to the MC fault zone and the placement of the first experiments within the MC fault zone, starting in spring 2024, has been assessed driven by the assessment of the structural inventory in close range around the existing Bedretto tunnel and permeability of

650   preferential flow paths. Some features of the MC fault zone are extensively presented in this paper (geological, rheological characterization), while others require further investigations in-situ and in the lab (frictional, hydraulic and poro-elastic characterization). Ongoing detailed exploration will focus onto the fault zone patches selected for experiments, providing insights into the distribution of geometrical-seismo-hydro-mechanical properties of the fault zone in higher spatial resolution. Although, the described procedure is specifically designed to a local challenge, we believe that the - in parts unusual - integrated, multidis-

655   ciplinary, multi-method and multi-scale approach executed here is of interest to other sites and experimental volumes elsewhere.

*Data availability.* The data supporting the discussion and conclusions presented in our article are available at the links referenced in the relevant papers we cite. Additionally, data can be requested from co-authors.

*Sample availability.* Samples will be available on request to the Bedretto Lab Rock Repository, bedrettolab@erdw.ethz.ch

660   *Author contributions.* All authors of this paper collectively contribute as a team of the FEAR/BULGG project. The role of each team member is described on the BedrettoLab website. Please use the following link: http://fear-earthquake-research.org/about/people/ last accessed:

2023-08-04. Specifically, AC, AZ, GP, JO, PAZ, WMB conducted the geological characterization. XM, FA conducted the geomechanics analysis. AS, DEB and MH conducted the geophysical characterization. AC, AS, DEB and WMB derived the geometrical model and forward simulations. DG, FA, MAM, MC and SW supervised the project, contributed to the experimental design and to the decision-making

665 associated with the multidisciplinary approach adopted for fault zone identification. All co-authors contributed to the writing of the paper.

*Competing interests.* The authors declare no competing interests.

*Acknowledgements.* Data and insights into the ongoing hydrogeological and geo-chemical investigations have been kindly provided by Dr. Brixel (Republic and Canton of Geneva) and Dr. Gholizadeh (ETHZ). The ortho-pictures and the DEM have been provided by Swisstopo through ETHZ. We thank also Prof. di Toro (Uni Padova), Prof. Herwegh (Uni Berne), and Prof. Emerit. Manktelow (ETHZ), and the FEAR

670 EAB for fruitful and interesting discussions. This project has received funding from the European Research Council (ERC) project FEAR (grant 856559) under the European Union's Horizon 2020 research and innovation program.

### References

Amann, F., Gischig, V., Evans, K., Doetsch, J., Jalali, R., Valley, B., Krietsch, H., Dutler, N., Villiger, L., Brixel, B., Klepikova, M., Kittilä, A., Madonna, C., Wiemer, S., Saar, M. O., Loew, S., Driesner, T., Maurer, H., and Giardini, D.: The seismo-hydromechanical behavior during deep geothermal reservoir stimulations: open questions tackled in a decameter-scale in situ stimulation experiment, Solid Earth, 9, 115–137, https://doi.org/10.5194/se-9-115-2018, 2018.

Arnet, M.: Deep Alpine Fluids: Origin, pathways and dynamic remobilisation in response to hydraulic stimulations at the Bedretto Underground Laboratory for Geoenergies (BULGG), https://doi.org/https://doi.org/10.3929/ethz-b-000532915, 2022.

Berger, A., Mercolli, I. P., Herwegh, M., and Gnos, E.: Geological map of the Aar massif and Tavetsch and Gotthard nappe, Geol Spec. Map 129 Explanatory Notes 129, 2017.

Bischoff, A., Heap, M. J., Mikkola, P., Kuva, J., Reuschlé, T., Jolis, E. M., Engström, J., Reijonen, H., and Leskelä, T.: Hydrothermally altered shear zones: A new reservoir play for the expansion of deep geothermal exploration in crystalline settings, Geothermics, 118, 102 895, https://doi.org/https://doi.org/10.1016/j.geothermics.2023.102895, 2024.

Braun, J.: PRECODE project: Rock-mechanical characterization of the candidate location for grout injections at Bedretto Laboratory, Switzerland, 2023.

Bröker, K. and Ma, X.: Estimating the Least Principal Stress in a Granitic Rock Mass: Systematic Mini-Frac Tests and Elaborated Pressure Transient Analysis, Rock Mechanics and Rock Engineering, 55, 1931–1954, https://doi.org/10.1007/s00603-021-02743-1, 2022.

Bukovská, Z., Soejono, I., Vondrovic, L., Vavro, M., Souček, K., Buriánek, D., Dobeš, P., Švagera, O., Waclawik, P., Řihošek, J., Verner, K., Sláma, J., Vavro, L., Koníček, P., Staš, L., Pécskay, Z., and Veselovský, F.: Characterization and 3D visualization of underground research facility for deep geological repository experiments: A case study of underground research facility Bukov, Czech Republic, Engineering Geology, 259, 105 186, https://doi.org/https://doi.org/10.1016/j.enggeo.2019.105186, 2019.

Caspari, E., Greenwood, A., Baron, L., Egli, D., Toschini, E., Hu, K., and Holliger, K.: Characteristics of a fracture network surrounding a hydrothermally altered shear zone from geophysical borehole logs, Solid Earth, 11, 829–854, https://doi.org/10.5194/se-11-829-2020, 2020.

Ceccato, A. and Pennacchioni, G.: Structural evolution of the Rieserferner pluton in the framework of the Oligo-Miocene tectonics of the Eastern Alps, Journal of Structural Geology, 116, 64–80, 2018.

Ceccato, A., Tartaglia, G., Antonellini, M., and Viola, G.: Multiscale lineament analysis and permeability heterogeneity of fractured crystalline basement blocks, Solid Earth, 13, 1431–1453, 2022.

Ceccato, A., Behr, W. M., Zappone, A. S., Tavazzani, L., and Giuliani, A.: Structural evolution, exhumation rates, and rheology of the European crust during Alpine collision: constraints from the Rotondo granite - Gotthard nappe, EOS Open Archives, https://doi.org/10.22541/au.170293691.11620931/v1, 2024.

Cheng, Y. and Renner, J.: Exploratory use of periodic pumping tests for hydraulic characterization of faults, Geophysical Journal International, 212, 543–565, https://doi.org/10.1093/gji/ggx390, 2017.

David, C., Nejati, M., and Geremia, D.: On petrophysical and geomechanical properties of Bedretto Granite, Tech. rep., ETH Zurich, 2020.

Dempsey, E., Holdsworth, R., Imber, J., Bistacchi, A., and Di Toro, G.: A geological explanation for intraplate earthquake clustering complexity: The zeolite-bearing fault/fracture networks in the Adamello Massif (Southern Italian Alps), Journal of Structural Geology, 66, 58–74, 2014.

Dobson, P., Kneafsey, T., Morris, J., Singh, A., Zoback, M., Roggenthen, W., Doe, T., Neupane, G., Podgorney, R., Wang, H., Knox, H., Schwering, P., Blankenship, D., Ulrich, C., Johnson, T., White, M., and the EGS Collab Team: The EGS Collab Hydroshear Experi-
710   ment at the Sanford Underground Research Facility – Siting Criteria and Evaluation of Candidate Sites, Geothermal Resources Council Transactions, 42, 16, https://www.geothermal-library.org/index.php?mode=pubs&action=view&record=1034004, 2018.

Dutler, N., Valley, B., Gischig, V., Villiger, L., Krietsch, H., Doetsch, J., Brixel, B., Jalali, M., and Amann, F.: Hydraulic fracture propagation in a heterogeneous stress field in a crystalline rock mass, Solid Earth Discuss., 2019, 1–41, https://doi.org/10.5194/se-2019-111, 2019.

Dutler, N. O., Valley, B., Amann, F., Jalali, M., Villiger, L., Krietsch, H., Gischig, V., Doetsch, J., and Giardini, D.: Poroe-
715   lasticity Contributes to Hydraulic-Stimulation Induced Pressure Changes, Geophysical Research Letters, 48, e2020GL091 468, https://doi.org/https://doi.org/10.1029/2020GL091468, 2021.

Escallon, D., Shakas, A., and Maurer, H.: Modelling and inferring fracture curvature from borehole GPR data: Case study from the Bedretto Laboratory, Switzerland, Near Surface Geophysics, https://doi.org/10.1002/nsg.12286, 2023.

Evans, K. F., Moriya, H., Niitsuma, H., Jones, R. H., Phillips, W. S., Genter, A., Sausse, J., Jung, R., and Baria, R.: Microseismicity and
720   permeability enhancement of hydrogeologic structures during massive fluid injections into granite at 3 km depth at the Soultz HDR site, Geophysical Journal International, 160, 388–412, https://doi.org/10.1111/j.1365-246X.2004.02474.x, 2005.

Fookes, P., Pettifer, G., and Waltham, T.: Geomodels in Engineering Geology: an Introduction, Whittles Publishing, 2015.

Gischig, V. S., Giardini, D., Amann, F., Hertrich, M., Krietsch, H., Loew, S., Maurer, H., Villiger, L., Wiemer, S., Bethmann, F., Brixel, B., Doetsch, J., Doonechaly, N. G., Driesner, T., Dutler, N., Evans, K. F., Jalali, M., Jordan, D., Kittilä, A., Ma, X., Meier, P., Nejati,
725   M., Obermann, A., Plenkers, K., Saar, M. O., Shakas, A., and Valley, B.: Hydraulic stimulation and fluid circulation experiments in underground laboratories: Stepping up the scale towards engineered geothermal systems, Geomechanics for Energy and the Environment, p. 100175, https://doi.org/https://doi.org/10.1016/j.gete.2019.100175, 2019.

Guglielmi, Y., Cappa, F., Avouac, J., Henry, P., and Elsworth, D.: Seismicity triggered by fluid injection-induced aseismic slip, Science, 348(6240), 1224–1226, https://doi.org/0.1126/science.aab0476, 2015a.

730   Guglielmi, Y., Henry, P., Nussbaum, C., Dick, P., Gout, C., and Amman, F.: Underground research laboratories for conducting fault activation experiments in shales, 2015b.

Guglielmi, Y., Birkholzer, J., Rutqvist, J., Jeanne, P., and Nussbaum, C.: Can fault leakage occur before or without reactivation? Results from an in situ fault reactivation experiment at Mont Terri, Energy Procedia, 114, 3167–3174, https://doi.org/10.1016/j.egypro.2017.03.1445, 2017.

735   Guglielmi, Y., Nussbaum, C., Jeanne, P., Rutqvist, J., Cappa, F., and Birkholzer, J.: Complexity of fault rupture and fluid leakage in shale: insights from a controlled fault activation experiment, Journal of Geophysical Research: Solid Earth, 125(2), 2169–9313, https://doi.org/10.1029/2019JB017781, 2020.

Guglielmi, Y., Cook, P., Soom, F., Schoenball, M., Dobson, P., and Kneafsey, T.: In Situ Continuous Monitoring of Borehole Displacements Induced by Stimulated Hydrofracture Growth, Geophysical Research Letters, 48, e2020GL090 782,
740   https://doi.org/https://doi.org/10.1029/2020GL090782, 2021.

Guillot, S. and Ménot, R.-P.: Paleozoic evolution of the external crystalline massifs of the Western Alps, Comptes Rendus Geoscience, 341, 253–265, 2009.

Hafner, S., Günthert, A., Burckhardt, C., Steiger, R., Hansen, J., and Niggli, C.: Geologischer atlas der schweiz 1: 25000, val bedretto, atlasblatt 68, Schweizerische Geologische Kommission, 1975.

745 Harms, U.: ICDP Primer - Planning, Managing, and Executing Continental Scientific Drilling Projects, 5th edition, https://doi.org/10.48440/icdp.2021.001, 2021.

Herwegh, M., Berger, A., Baumberger, R., Wehrens, P., and Kissling, E.: Large-scale crustal-block-extrusion during late Alpine collision, Scientific Reports, 7, 1–10, 2017.

Herwegh, M., Berger, A., Glotzbach, C., Wangenheim, C., Mock, S., Wehrens, P., Baumberger, R., Egli, D., and Kissling, E.: Late stages of
750     continent-continent collision: Timing, kinematic evolution, and exhumation of the Northern rim (Aar Massif) of the Alps, Earth-Science Reviews, 200, 102 959, 2020.

Hunt, R.: Geotechnical Engineering Investigation Handbook, Second Edition, Taylor Francis, 2005.

Häring, M. O., Schanz, U., Ladner, F., and Dyer, B. C.: Characterisation of the Basel 1 enhanced geothermal system, Geothermics, 37, 469–495, https://doi.org/https://doi.org/10.1016/j.geothermics.2008.06.002, 2008.

755 Jalali, M., Gischig, V., Doetsch, J., Näf, R., Krietsch, H., Klepikova, M., Amann, F., and Giardini, D.: Transmissivity Changes and Microseismicity Induced by Small-Scale Hydraulic Fracturing Tests in Crystalline Rock, Geophysical Research Letters, 45, 2265–2273, https://doi.org/https://doi.org/10.1002/2017GL076781, 2018.

Jeanne, P., Guglielmi, Y., Lamarche, J., Cappa, F., and Marié, L.: Architectural characteristics and petrophysical properties evolution of a strike-slip fault zone in a fractured porous carbonate reservoir, Journal of Structural Geology, 44, 93–109,
760     https://doi.org/10.1016/j.jsg.2012.08.016, 2012.

Kakurina, M., Guglielmi, Y., Nussbaum, C., and Valley, B.: Slip perturbation during fault reactivation by a fluid injection, Tectonophysics, 757, 140–152, https://doi.org/10.1016/j.tecto.2019.01.017, 2019.

Kickmaier, W. and McKinley, I.: A review of research carried out in European rock laboratories, Nuclear Engineering and Design, 176, 75–81, 1997.

765 Kiliç, T., Kartal, R. F., Kadirioğlu, F. T., Bohnhoff, M., Nurlu, M., Acarel, D., Martínez Garzon, P., Dresen, G., Özsarac, V., and Malin, P. E.: Geophysical Borehole Observatory at the North Anatolian Fault in the Eastern Sea of Marmara (GONAF): initial results, Journal of Seismology, 24, 375–395, https://doi.org/10.1007/s10950-020-09907-6, 2020.

Kim, G. Y., Kim, K., Lee, J.-Y., Cho, W.-J., and Kim, J.-S.: Current Status of the KURT and Long-term In-situ Experiments, Journal of the Korean Society of Mineral and Energy Resources Engineers, 54, 344–357, 2017.

770 Kralik, M., Clauer, N., Holnsteiner, R., and Kappel, F.: Recurrent fault activity in the Grimsel Test Site (GTS, Switzerland): revealed by Rb-Sr, K-Ar and tritium isotope techniques, Journal of the Geological Society, London, 149, 293–301, https://doi.org/10.1144/gsjgs.149.2.0293, 1992.

Krietsch, H., Gischig, V. S., Doetsch, J., Evans, K. F., Villiger, L., Jalali, M., Valley, B., Löw, S., and Amann, F.: Hydromechanical processes and their influence on the stimulation effected volume: observations from a decameter-scale hydraulic stimulation project, Solid Earth, 11,
775     1699–1729, https://doi.org/10.5194/se-11-1699-2020, 2020a.

Krietsch, H., Villiger, L., Doetsch, J., Gischig, V., Evans, K. F., Brixel, B., Jalali, M. R., Loew, S., Giardini, D., and Amann, F.: Changing Flow Paths Caused by Simultaneous Shearing and Fracturing Observed During Hydraulic Stimulation, Geophysical Research Letters, 47, e2019GL086 135, https://doi.org/https://doi.org/10.1029/2019GL086135, 2020b.

Kwiatek, G., Plenkers, K., Dresen, G., and Group, J. R.: Source Parameters of Picoseismicity Recorded at Mponeng Deep Gold
780     Mine, South Africa: Implications for Scaling Relations, Bulletin of the Seismological Society of America, 101, 2592–2608, https://doi.org/10.1785/0120110094, 2011.

Ledésert, B., Hebert, R., Genter, A., Bartier, D., Clauer, N., and Grall, C.: Fractures, hydrothermal alterations and permeability in the Soultz Enhanced Geothermal System, Comptes Rendus Geoscience, 342, 607–615, https://doi.org/https://doi.org/10.1016/j.crte.2009.09.011, vers l'exploitation des ressources géothermiques profondes des systèmes hydrothermaux convectifs en milieux naturellement fracturés, 2010.

785 Lesko, K.: The Sanford Underground Research Facility at Homestake (SURF), Physics Procedia, 61, 542–551, https://doi.org/10.1016/j.phpro.2014.12.001, 2015.

Lützenkirchen, V. H. and Loew, S.: Late Alpine brittle faulting in the Rotondo granite (Switzerland): deformation mechanisms and fault evolution, Swiss Journal of Geosciences, 104, 31–54, https://doi.org/10.1007/s00015-010-0050-0, 2011.

790 Ma, K.-F., Tanaka, H., Song, S.-R., Wang, C.-Y., Hung, J.-H., Tsai, Y.-B., Mori, J., Song, Y.-F., Yeh, E.-C., Soh, W., Sone, H., Kuo, L.-W., and Wu, H.-Y.: Slip zone and energetics of a large earthquake from the Taiwan Chelungpu-fault Drilling Project, Nature, 444, 473–476, https://doi.org/10.1038/nature05253, 2006.

Ma, X., Hertrich, M., Amann, F., Bröker, K., Gholizadeh Doonechaly, N., Gischig, V., Hochreutener, R., Kästli, P., Krietsch, H., and Marti, M.: Multi-disciplinary characterizations of the BedrettoLab–a new underground geoscience research facility, Solid Earth, 13, 301–322, 795 2022.

Meier, M.: Time to Make Faults Move, 2024.

Munro, M. A. and Blenkinsop, T. G.: MARD—A moving average rose diagram application for the geosciences, Computers & Geosciences, 49, 112–120, 2012.

Niemeijer, A. and Spiers, C.: A microphysical model for strong velocity weakening in phyllosilicate-bearing fault gouges, Journal of Geo-800 physical Research: Solid Earth, 112, 2007.

Ofterdinger, U. S., Renard, P., and Loew, S.: Hydraulic subsurface measurements and hydrodynamic modelling as indicators for groundwater flow systems in the Rotondo granite, Central Alps (Switzerland), Hydrological Processes, 28, 255–278, https://doi.org/https://doi.org/10.1002/hyp.9568, 2014.

Olsson, O., Falk, L., Forslund, O., Lundmark, L., and Sandberg, E.: Borehole radar applied to the characterization of hydraulically conductive 805 fracture zones in crystalline rock 1, Geophysical prospecting, 40, 109–142, 1992.

Ophori, D. U., Stevenson, D., Gascoyne, M., Brown, A., Davison, C., Chan, T., and Stanchell, F.: Revised model of regional groundwater flow of the Whiteshell Research Area: Summary, 1995.

Osten, J.: Hydro-mechanical characterization of candidate fault zones for FEAR in the Bedretto Tunnel, Switzerland, 2022.

Osten, J., Schaber, T., Gaus, G., Hamdi, P., Amann, F., and Achtziger-Zupancičič, P.: A multi-method investigation of the permeability 810 structure of brittle fault zones with ductile precursors in crystalline rock, Grundwasser, https://doi.org/10.1007/s00767-023-00561-6, 2024.

Pennacchioni, G., Ceccato, A., Fioretti, A. M., Mazzoli, C., Zorzi, F., and Ferretti, P.: Episyenites in meta-granitoids of the Tauern Window (Eastern Alps): unpredictable?, Journal of Geodynamics, 101, 73–87, 2016.

Pleuger, J., Mancktelow, N., Zwingmann, H., and Manser, M.: K–Ar dating of synkinematic clay gouges from Neoalpine faults of the Central, Western and Eastern Alps, Tectonophysics, 550, 1–16, 2012.

815 Rast, M., Galli, A., Ruh, J. B., Guillong, M., and Madonna, C.: Geology along the Bedretto tunnel: kinematic and geochronological constraints on the evolution of the Gotthard Massif (Central Alps), Swiss Journal of Geosciences, 115, 8, https://doi.org/10.1186/s00015-022-00409-w, 2022.

Sakuma, H., Sugihara, K., Koide, K., Mikake, S., and Bäckblom, G.: The Mizunami underground research laboratory in Japan-programme for study of the deep geological environment, 1998.

820  Schill, E., Meixner, J., Meller, C., Grimm, M., Grimmer, J., Stober, I., and Kohl, T.: Criteria and geological setting for the generic geothermal underground research laboratory, GEOLAB, Geothermal Energy, 4, https://doi.org/10.1186/s40517-016-0049-5, 2016.

Schneeberger, R., Kober, F., Spillmann, T., Blechschmidt, I., and Lanyon, G. W.and Mäder, U. K.: Grimsel Test Site: Revisiting the site-specific geoscientific knowledge, Nagra Technical Report, NTB 19-01, 2019.

Schneider, T.: Basistunnel Furka—Geologische Aufnahme des Fensters Bedretto, Brig, Furka-Oberalp-Bahn AG, 1985.

825  Shakas, A. and Linde, N.: Effective modeling of ground penetrating radar in fractured media using analytic solutions for propagation, thin-bed interaction and dipolar scattering, Journal of Applied Geophysics, 116, 206–214, 2015.

Shakas, A., Maurer, H., Giertzuch, P.-L., Hertrich, M., Giardini, D., Serbeto, F., and Meier, P.: Permeability enhancement from a hydraulic stimulation imaged with Ground Penetrating Radar, Geophysical Research Letters, 47, e2020GL088 783, 2020.

Shapiro, S. A., Kummerow, J., Dinske, C., Asch, G., Rothert, E., Erzinger, J., Kümpel, H.-J., and Kind, R.: Fluid induced seismicity guided
830   by a continental fault: Injection experiment of 2004/2005 at the German Deep Drilling Site (KTB), Geophysical Research Letters, 33, 0094–8276, https://doi.org/10.1029/2005GL024659, 2006.

Siren, T.: Overview of Finnish Spent Nuclear Fuel Disposal Programme, Journal of the Korean Society of Mineral and Energy Resources Engineers, 54, 367–376, 2017.

Sutherland, R., Toy, V., Townend, J., Cox, S., Eccles, J., Faulkner, D., Prior, D., Norris, R., Mariani, E., Boulton, C., Carpenter, B., Menzies,
835   C., Little, T., Hasting, M., De Pascale, G., Langridge, R., Scott, H., Lindroos, Z. R., Fleming, B., and Kopf, A.: Drilling reveals fluid control on architecture and rupture of the Alpine fault, New Zealand, Geology, 40(12), 1143–1146, https://doi.org/10.1130/G33614.1, 2012.

Tobin, H. J., Saffer, D. M., Castillo, D. A., and Hirose, T.: Direct constraints on in situ stress state from deep drilling into the Nankai subduction zone, Japan, Geology, 50(11), 1229–123, https://doi.org/10.1130/G49639.1, 2022.

840  Ustaszewski, M. E., Hampel, A., and Pfiffner, O. A.: Composite faults in the Swiss Alps formed by the interplay of tectonics, gravitation and postglacial rebound: an integrated field and modelling study, Swiss Journal of Geosciences, 101, 223–235, 2008.

Villiger, L., Gischig, V. S., Doetsch, J., Krietsch, H., Dutler, N. O., Jalali, M., Valley, B., Selvaduai, P. A., Mignan, A., Plenkers, K., Giardini, D., Amann, F., and Wiemer, S.: Influence of reservoir geology on seismic response during decameter scale hydraulic stimulations in crystalline rock Project: Grimsel In Situ Stimulation and Circulation (ISC) Experiment, Solid Earth, 11, 627–655, https://doi.org/10.5194/se-
845   11-627-2020, 2020.

Villiger, L., Gischig, V. S., Kwiatek, G., Krietsch, H., Doetsch, J., Jalali, M., Amann, F., Giardini, D., and Wiemer, S.: Metre-scale stress heterogeneities and stress redistribution drive complex fracture slip and fracture growth during a hydraulic stimulation experiment, Geophysical Journal International, 225, 1689–1703, https://doi.org/10.1093/gji/ggab057, 2021.

Volpe, G., Pozzi, G., Collettini, C., Spagnuolo, E., Achtziger-Zupančič, P., Zappone, A., Aldega, L., Meier, M., Giardini, D., and Cocco,
850   M.: Laboratory simulation of fault reactivation by fluid injection and implications for induced seismicity at the BedrettoLab, Swiss Alps, Tectonophysics, 862, 229 987, https://doi.org/https://doi.org/10.1016/j.tecto.2023.229987, 2023.

Vomvoris, S., Kickmaier, W., and McKinley, I.: Grimsel Test Site: 20 Years of Research in Fractured Crystalline Rocks—Experience Gained and Future Needs, DYNAMICS OF FLUIDS IN FRACTURED ROCK, p. 14, 2004.

Weisenberger, T. and Bucher, K.: Zeolites in fissures of granites and gneisses of the Central Alps, Journal of metamorphic Geology, 28,
855   825–847, 2010.

Wenning, Q. C., Madonna, C., de Haller, A., and Burg, J.-P.: Permeability and seismic velocity anisotropy across a ductile–brittle fault zone in crystalline rock, Solid Earth, 9, 683–698, https://doi.org/10.5194/se-9-683-2018, 2018.

Zhang, S., Ma, X., Bröker, K., van Limborgh, R., Wenning, Q., Hertrich, M., and Giardini, D.: Fault Zone Spatial Stress Variations in a Granitic Rock Mass: Revealed by Breakouts Within an Array of Boreholes, Journal of Geophysical Research: Solid Earth, 128, e2023JB026 477, https://doi.org/https://doi.org/10.1029/2023JB026477, 2023.

Zoback, M., Hickman, S. H., and Ellsworth, W.: Scientific Drilling Into the San Andreas Fault Zone — An Overview of SAFOD's First Five Years, Scientific Drilling, 11(1), https://doi.org/10.2204/iodp.sd.11.02.201, 2011.